On the nucleation and interaction mechanisms of hexagonal close packed (HCP) martensite in a $Fe_{50}Mn_{30}Co_{10}Cr_{10}$ high entropy alloy

Lipeng Ding[a,b], Yanxiang Liang[c,*], Yaoyao Weng[d], Jian Tu[e,*], Zhihong Jia[a, d], Qing Liu[a,d], Thomas Pardoen[f], Hosni Idrissi[f,*]

[a] Key laboratory for Light-weight Materials, Nanjing Tech University, Nanjing 211816, PR China

[b] Suzhou Laboratory, 215125, Suzhou, China

[c] State Key Laboratory of Rail Transit Vehicle System, Southwest Jiaotong University, Chengdu 610031, China

[d] School of Materials Science and Engineering, Nanjing Institute of Technology, Nanjing 211167, China

[e] College of Material Science and Engineering, Chongqing University of Technology, Chongqing, 400054, PR China

[f] UCLouvain, Institute of Mechanics Materials and Civil Engineering, IMAP, 1348 Louvain-la-Neuve, Belgium

Corresponding author

Yanxiang Liang: liangyx@swjtu.edu.cn; Jian Tu: tujian@cqut.edu.cn; Hosni Idrissi: hosni.idrissi@uclouvain.be

Abstract

The nucleation and interaction mechanisms of hexagonal close packed (ε-HCP) martensite in a $Fe_{50}Mn_{30}Co_{10}Cr_{10}$ high entropy alloy were investigated using atomic-resolution scanning transmission electron microscopy and molecular dynamic simulations. We demonstrate that the nucleation of ε-HCP is controlled by the activation of different mechanisms, including the six-plane and stair-rod cross-slip mechanisms. The nature of the intricate interaction mechanisms between two conjugated ε lamellae are highly dependent on the level of deformation and on the difference of thickness between the two crossing ε-HCP. Various absorption and transmission mechanisms of the incoming ε-HCP across the primary ε-HCP are revealed, involving local lattice rotation, the formation of new boundaries as well as stress induced twinning and phase transformation at the intersection sites. The synergy/competition between these mechanisms is discussed and compared

with recent literature. These findings shed new light on the elementary mechanisms at the origin the remarkable strain hardening capacity of this category of high entropy alloys.

Key words: High-entropy alloys; Martensite; Transmission electron microscopy (TEM); Plasticity

1. Introduction

Non-equiatomic high entropy alloys (HEAs) with dual- or multi-phase structures are of particular interest owing to their significantly enhanced strain hardening capacity compared to the more stable equiatomic reference HEA [1, 2]. Among various non-equiatomic HEAs, the $Fe_{50}Mn_{30}Co_{10}Cr_{10}$ metastable dual-phase high entropy alloy (DP-HEA), recently designed by Li et al. [3], has received special attention due to its excellent combination of strength (UTS ~ 850MPa) and ductility (elongation ~ 70%). Such excellent performances are very much associated to a high strain hardening capacity that contributes at both raising the strength/hardness and the resistance to plastic localization. This is mainly attributed to the activation of two deformation modes: interface hardening due to the dual-phase microstructure and transformation induced plasticity (TRIP) effect from γ (FCC) to ε (HCP) phase upon deformation [4, 5]. The interfaces resulting from the formation of a high density of hexagonal ε-martensite bands acts as effective barriers for dislocation slip since slip transmission at the FCC/HCP phase boundary requires the activation of non-basal <c + a> dislocations at higher critical stress [6].

Recently, the deformation behavior of the DP-HEA has been extensively investigated in the literature. Li et al. [4] studied the deformation mechanisms using electron backscatter diffraction (EBSD) and electron channeling contrast imaging (ECCI). At the early stage of deformation, plastic deformation is mainly accommodated by the FCC γ matrix, including displacive transformation from γ to ε, stacking faults and dislocation slip. At the later stages of deformation, additional mechanical twinning, dislocation slip and stacking faults are activated within the ε-HCP phase. Moreover, Lu et al. [5] reported a new mechanism, referred to as the “bidirectional transformation induced plasticity” (B-TRIP), achieved by dynamic forward transformation from γ-FCC to ε-HCP and dynamic reverse transformation from ε-HCP to γ-FCC, providing extensive work hardening capacity without sacrificing ductility. Through in-situ tensile testing and transmission electron microscopy (TEM) characterizations, Bu et al. [6] reported the activation of a high fraction of non-basal <c+a> dislocations allowing for frequent double cross-slip which explains the high

deformability of this class of HEAs. However, the elementary mechanisms controlling the nucleation of ε-HCP phase did not receive sufficient attention, although such behavior is critical for tailoring the mechanical properties. Furthermore, the interaction mechanisms between the multiple ε-HCP variants in these alloys, which is expected to play a pivotal role in strain hardening remains, to a wide extent, unclear.

The transformation γ→ε can be achieved through the highly coordinated glide of 1/6<112> Shockley partial dislocations (SPDs) on alternate close packed {111} planes [7]. More fundamentally, how ε-HCP nucleate from specific arrangements of partial dislocations is a critical issue. As for now, several fundamental mechanisms for ε-HCP nucleation have been proposed and can be categorized into three main groups: (i) the *pole mechanism*, involving continuous transformation around the pole Frank partial and the sweep of SPDs around the pole [8]; (ii) the *stair-rod cross-slip mechanism*. In this case, the leading SPD can dissociate under high stress on the primary slip plane into a stair-rod dislocation and another glissile SPD on the conjugate plane. ε-HCP can thus be formed if this process is repeated at every second layers [9]; (iii) the *six-layer mechanism*, involving the interaction of two co-planar perfect dislocations which lead to the formation of three SPDs on every second close packed {111} plane, forming a six-layer ε-HCP crystal [10]. In the literature, the fundamental mechanisms controlling the nucleation of ε-HCP phase have been extensively studied in conventional alloys based on a single host metal, such as TRIP steels [7, 11, 12]. However, such phenomenon is seldomly addressed in high entropy alloys. Given the highly distorted lattice structures and compositional complexity of high entropy alloys, it can be anticipated that the activation of partial dislocations and the nucleation of the HCP phase is intrinsically different when compared to conventional alloys. Wang et al. [13] studied the phase transformation in a $Fe_{49.5}Mn_{30}Co_{10}Cr_{10}C_{0.5}$ alloy and suggested that the six-layer mechanism proposed by Mahajan et al. [10] is responsible for the nucleation of HCP in this alloy, however without experimental substantiation. Wang et al. [14] proposed that, instead of the six-layer mechanism, the cross-slip stair-rod mechanism proposed by Fujita and Ueda [9] is responsible for the nucleation of the ε-HCP in the same alloy under cryogenic conditions. However, the nature of the defects involved at the very early stage of the HCP martensite nucleation is still elusive.

The interaction mechanisms between different ε-HCP variants have been studied in high interstitial-alloyed austenitic steels and shape memory alloys [15-18]. Various ε-ε intersection

products, such as α′-martensite, secondary ε phase, ε twins and γ twins have been observed in different austenitic alloys. Yang et al. [19] reported the formation of a new ε-HCP variant at the intersections of the two initial HCP bands in a Fe-based shape memory alloys. This change of orientation which can be conveniently described as rigid-body rotation mechanism is attributed to the cooperative shear associated with the initial two HCP variants. Lee et al. [20] reported that the interactions of two HCP variants serve as nucleation sites for α′-martensite in an austenitic 18Cr–10Mn–0.4N steel. Zhang et al. [16] showed the formation of ε twins of $\{10\bar{1}2\}$ and $\{1011\}$ types at the two HCP variants intersection sites in Fe-30Mn-6Si shape memory alloy. Recently, Su et al. [21] studied the bidirectional martensite transformation in a carbon-doped DP-HEA. These authors demonstrated the deformation-induced reverse transformation from ε-HCP back to γ-FCC phase at the intersection of two crossing HCP variants owing to the interaction of pyramidal slip and pre-existing stacking faults, leading to new partial dislocations and the formation of FCC phase. No body centered or tetragonal α′ phase is observed in this case. Therefore, the interaction mechanisms of HCP variants in HEAs are different from conventional alloys. However, as for the nucleation of HCP phase, the ε-ε interaction mechanisms in DP-HEAs are still poorly understood. Furthermore, most of previous investigations of the nature of ε-ε interaction mechanisms were conducted by EBSD and diffraction contrast TEM imaging while atomic-scale characterization of these mechanisms can be hardly found in the literature.

The present work aims at revealing the nanoscale nucleation and interaction mechanisms of hexagonal close packed ε-martensite in a $Fe_{50}Mn_{30}Co_{10}Cr_{10}$ high entropy alloy at different strain levels. Conventional diffraction contrast imaging, aberration-corrected scanning transmission electron microscopy (STEM) and molecular dynamic (MD) simulations were used to unravel the atomic structure of the defects involved at the onset of ε-HCP band as well as the characteristics of ε-ε intersection regions.

2. Methods

2.1 Experimental procedure

The button-shaped ingot of $Fe_{50}Mn_{30}Co_{10}Cr_{10}$ (at. %) HEA was produced by arc-melting pure iron, manganese, chromium and cobalt (over 99.9 wt %) under a high-purity argon atmosphere. The as-cast samples were subjected to hot compression at a temperature of 1000ºC with 70 % thickness

boundary condition along x and y direction. The model systems were deformed at 300 K under a constant deformation rate $\dot{F} = \begin{pmatrix} 0 & 1 & 0 \\ 0 & 0 & 0 \\ 0 & 0 & 0 \end{pmatrix} \dot{\gamma}_0$, where $\dot{\gamma}_0 = 1\times10^8\ s^{-1}$. In the simulations, the NPT ensemble (constant number of particles, pressure, and temperature) was systematically employed to maintain pressure equilibrium during deformation. For atomic modeling, the atoms of each type were randomly distributed within the crystal lattice according to the predefined stoichiometric ratios.

3. Results

3.1 Initial microstructure

Stress strain curves providing the mechanical response in uniaxial tension are provided in Appendix. The uniform elongation is 51% signaling a high to very high strain hardening exponent. Fig.1 shows a typical series of characterization results generated for the as-homogenized DP-HEA. The BSE-SEM micrograph of Fig. 1(a) and the EBSD maps of Fig. 1(c, d) exhibit the expected dual-phase microstructure, namely FCC-γ (67.9%) matrix, HCP ε-phase (23.8%) and equiaxed grains with an average size of ~ 23μm. The grain boundary (GB) map of Fig. 1(d) shows that, in addition to annealing twin boundaries (TBs), 70.5° <11$\bar{2}$0> phase boundaries in ε-phase are observed (PBs shown as blue lines), accounting for 56.4% of the total number of the boundaries, see insert of Fig. 1(d). In the bright-field TEM (BF-TEM) micrograph shown in Fig. 1(e), a high density of stacking faults (SFs) is observed in the FCC-γ phase. Enlarged BF-TEM micrograph and atomic-resolution STEM micrograph of one of these SFs are presented in Fig. 1(e and f). The later shows an intrinsic SF (ISF) formed by the glide of a single 1/6 <112> SPD in {111} plane.

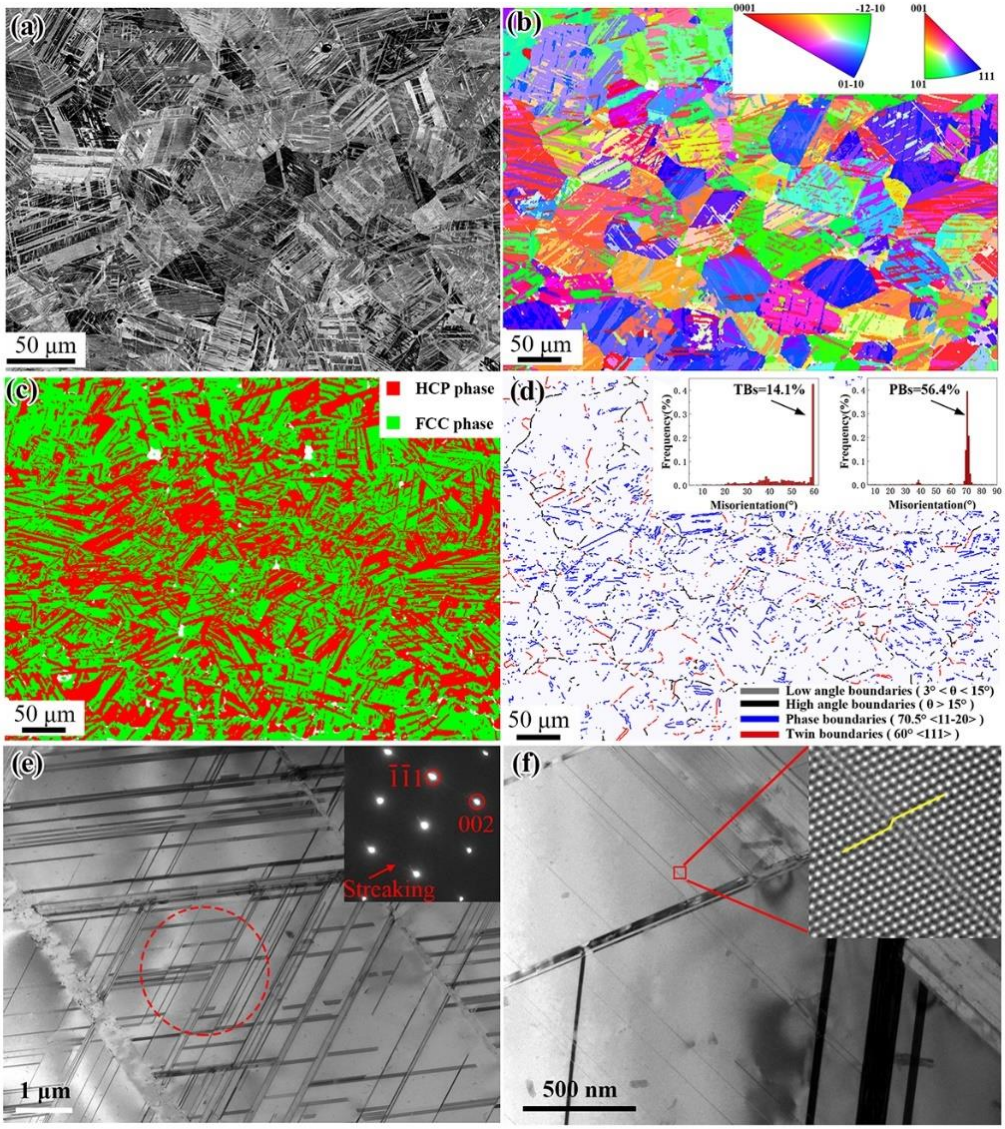

Fig. 1(a) BSE-SEM micrograph and (b-d) EBSD analysis of as-homogenized DP-HEA. (b) inverse pole figure (IPF) map indicating crystallographic orientation; (c) phase map revealing a dual-phase microstructure, i.e., γ in blue, ε in red; (d) grain boundary (GB) map showing twin boundaries (60◦<111>, TBs) and phase boundaries (70.5◦/<11$\bar{2}$0>, PBs); a misorientation angle histogram is inserted in the corner of (d). (e) BF-TEM micrograph of SFs with corresponding SAED pattern obtained at <110>$_\gamma$ zone axis. (f) enlarged BF-TEM micrograph with atomic resolution HAADF-STEM micrograph of one SFs in the top right inset.

3.2 Deformed microstructure

BF-TEM micrographs of Fig. 2 illustrate the evolution of the microstructure in the FCC-γ matrix with increasing deformation. At ε=0.02 (Fig. 2(a)), except for a slight increase of SF density,

the microstructure does not exhibit clear differences when compared to the as-homogenized sample. Note the formation of SFs at different {111} planes which lead to numerous stair-rod dislocations (marked by red arrows in Fig. 2(a)). These SFs can be clearly distinguished after tilting the TEM foil away from the [110] zone axis (Fig. 2(b)). Stair-rod dislocations and the associated SFs act as strong barriers for dislocation motion, hence potentially promoting strain hardening. Very few perfect dislocations are found due to the rather low stacking fault energy of this alloy. At ε=0.1, a high density of thin lamellae is formed as shown in Fig. 2(c, d). These lamellae are identified as mechanically-induced ε-HCP martensite as shown in the inserted SAED pattern. Multiple ε-HCP variants lying on different planes show up at ε=0.2 (see the BF-TEM micrograph of Fig. 2(e) and the corresponding SAED pattern in the inset). At ε=0.3, deformation bands with different orientations dominate the microstructure. Most of these bands are identified as ε-HCP as evidenced by the inserted SAED, indicating that most of the γ-FCC grains have been transformed to ε-HCP. The deformation products formed in the ε-HCP martensite is shown in supplementary materials Fig. S1, which indicates dislocation slip is the main deformation mechanism in the ε-HCP phase.

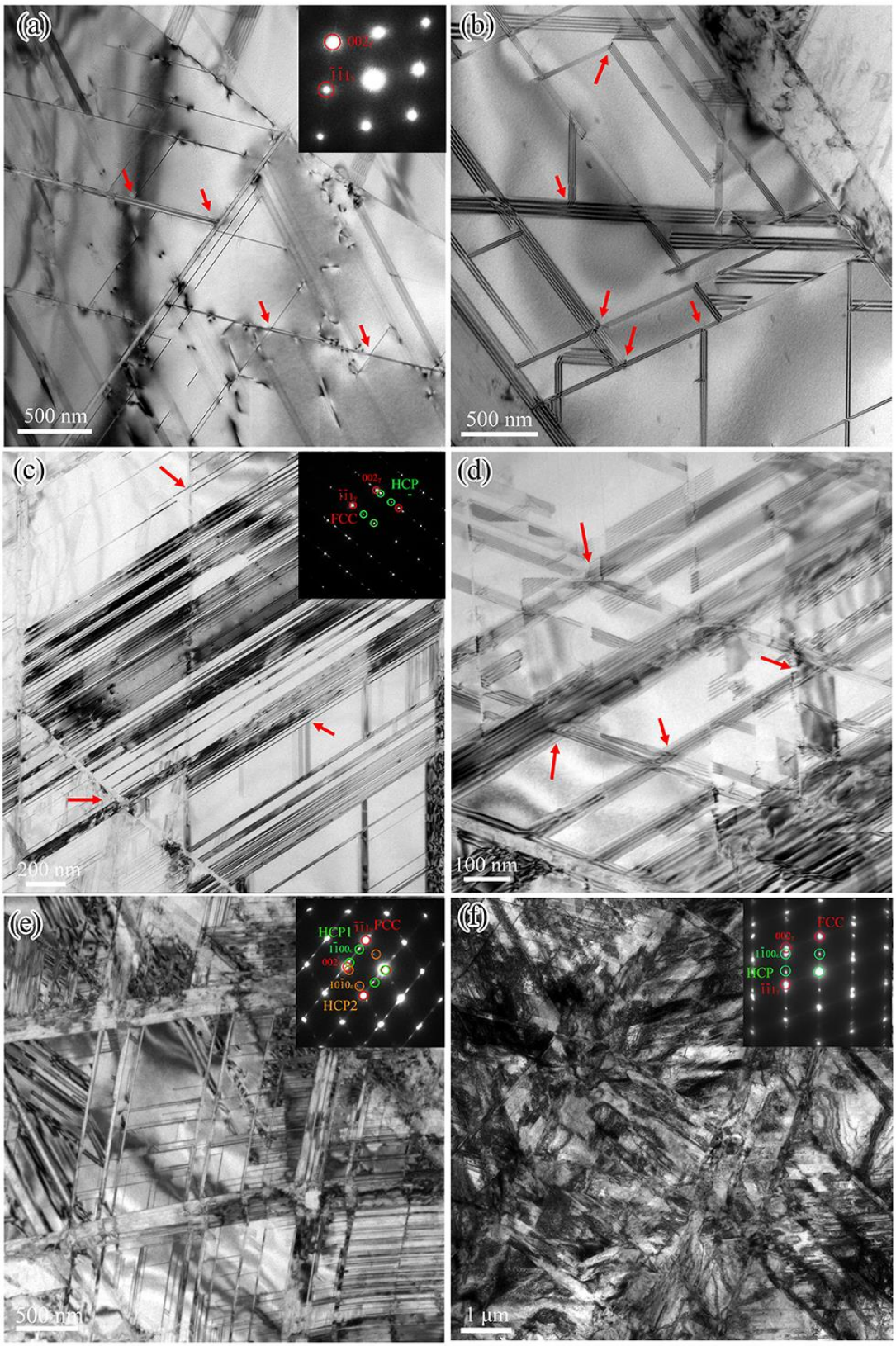

Fig. 2 Typical microstructures of the samples deformed at (a, b) ε=0.02, (c, d) ε=0.1, (e) ε=0.2 and (f) ε=0.3 obtained at <110>$_\gamma$ zone axis. The corresponding SAED patterns of (a, c, e, f) are inserted

in the right corners. The interaction sites between planar defects lying in different planes are marked by red arrows. The SAED in (e) confirms the activation of multiple ε-HCP variants.

3.3 Nucleation mechanisms of ε-HCP

The nucleation mechanisms of the ε-HCP lamellas were investigated in the specimen deformed up to ε=0.1. Fig. 3(a) exhibits high resolution STEM micrograph of a planar defect identified as a six-layer HCP embryo formed by three SFs on alternate close packed {111} planes. Enlarged images at the extremities of this defect (delimited by red dashed rectangle in Fig. 3(b-c)) show partial dislocations. The method developed by Howe [25] was used to identify the Burgers vectors of the partials of Fig. 3(b), see the red circuit in this figure. The closure failure vectors $\overline{\mathrm{FSe}}$ and $\overline{\mathrm{FSs}}$ are measured as one and two lattice spacings, suggesting the presence of two 30° SPDs and one 90° SPD. The net Burgers vector of the three partials is zero ($b_1+b_2+b_3=0$) as evidenced by the Burgers circuit with no closure failure (dashed red line). On the opposite side of the ε-HCP embryo (Fig. 3(c)), the three partials located at different planes are associated to 6-layer ε → 4-layer ε, 4-layer ε → ISF and ISF → γ matrix transformations. All the three partials are identified as 1/6$[\bar{2}11]$ (30°) SPDs as evidenced by the Burgers circuits shown in Fig. 3(c). These observations confirm that the six-layer mechanism proposed by Mahajan and Chin [10] is responsible for the nucleation of 6-layer ε-HCP embryo. This involves the interaction of two co-planar perfect dislocations leading to the formation of three SPDs on alternate $(\bar{1}\bar{1}1)$ plane following the reaction:

$$\frac{1}{2}[\bar{1}01]_{(\bar{1}\bar{1}1)} + \frac{1}{2}[011]_{(\bar{1}\bar{1}1)} \rightarrow 3 \times \frac{1}{6}[\bar{1}21]_{(\bar{1}\bar{1}1)} \qquad (1)$$

Atomic resolution HAADF-STEM imaging was also performed at the intersection of two inclined planar defects to investigate the role of multiple slip on ε-HCP nucleation. In Fig. 3(d), ISFs lying in the $(\bar{1}11)$ and $(\bar{1}\bar{1}1)$ planes are connected by a stair-rod dislocation. One leading partial (marked by red dashed circle) dragging an inclined ISF stopped at the vicinity of the horizontal ISF. Fig. 3(e) shows the interaction of one ISF in the (111) plane with another one in the $(\bar{1}\bar{1}1)$ plane leading to the formation of a stair-rod dislocations and new glissile partial in the $(\bar{1}\bar{1}1)$ plane, transforming the ISF into a 4-layer ε-HCP band. This can occur by the stair-rod cross-slip mechanism proposed by Mori and Fujita following the equation [9]:

$$\frac{1}{6}[\bar{2}11]_{(111)} \rightarrow \frac{1}{6}[\overline{11}1]_{sessile} + \frac{1}{6}[\bar{1}21]_{(\bar{1}\bar{1}1)} \qquad (2)$$

Schematic illustrations of the six-layer mechanism and stair-rod cross-slip mechanism are displayed in Fig. 3(f, g).

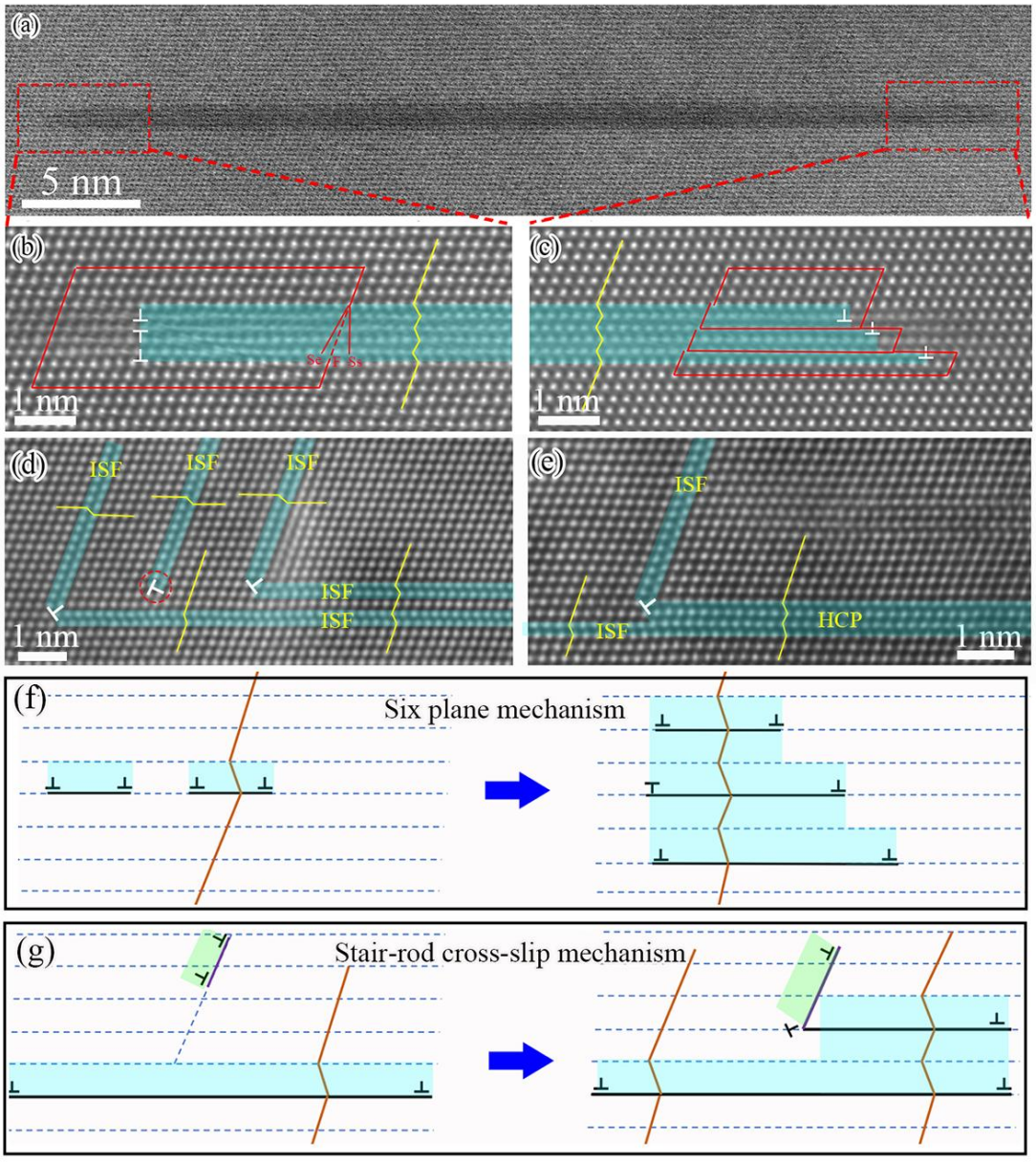

Fig. 3 (a) Low magnification <110>$_\gamma$ STEM micrograph of a planar defect in sample deformed at ε=0.1, (b, c) show enlarged images of the dislocations delimiting this defect, marked by red dashed rectangles in (a). (d, e) STEM micrographs showing the nucleation of HCP phase by the stair-rod cross-slip mechanism, (f, g) are schematic illustrations of the six plane and stair-rod cross-slip mechanisms, respectively.

3.3 Intersection between ε-HCP

Various ε-ε interactions have been observed for the sample deformed to ε=0.1. At this stage,

most of the inclined ε-HCP bands have not penetrated through the primary ε-HCP bands. The ε-ε interaction products appear to depend on the thickness difference between the two ε-HCP variants. When the two crossing ε-HCP variants exhibit significant thickness difference, the incident inclined ε-HCP lamellae are blocked or form a new interface with the primary ε-HCP laminate. Figs. 4(a, b, c) show the interaction between a four-layer ε-HCP with thicker ε-HCP lamellae. In Fig. 4(a), the leading partials of the 4-layer incident ε-HCP are stopping ahead of the primary ε-HCP band with no local growth of this band at the intersection site. In Fig. 4(b), two leading partials reacted with the interface, leading to the formation of two stair-rod dislocations at the intersection site and two partial dislocations which moved to the right side, following reaction (2). Note that the angle formed by the two variants is equal to 71°, leading to an acute-angled V-shaped configuration. However, for unknown reasons, the dissociation cross-slip reactions did not occur every two {111} planes, leading to defective ε-HCP with local increase of the thickness of the primary ε-HCP laminate by five {111} layers. In Fig. 4(c), the two incoming partials of the inclined ε-HCP embryo were forced to interact with the primary ε-HCP band, leading to the formation of two stair-rod sessile dislocations and two glissile partials which moved to the left side. In this case, the angle is 109° (obtuse-angled V-shaped configuration) and the reaction is:

$$\frac{1}{6}[\bar{2}11]_{(111)} \rightarrow \frac{1}{3}[0\bar{1}0]_{sessile} + \frac{1}{6}[\overline{11}2]_{(\overline{1}\overline{1}1)} \qquad (3)$$

The following examples provide insight on the interaction mechanisms between ε-HCP bands with higher thicknesses. For the inclined 16-layer ε-HCP band shown in Fig. 4(d), only four leading partials interact with the primary ε-HCP band. This led to the formation of four stair-rod dislocations at the intersection and the thickening of the primary ε-HCP by 8-layer, while 5 partials stopped ahead of the primary ε-HCP. This can be explained by the fact that these partials were nucleated from different sources, which could lead to higher repulsive interactions between these partials and the stair-rod dislocations. For the inclined 16-layer ε-HCP shown in Fig. 4(e), two partials interacted with the interface leading to the thickening the primary ε-HCP by 4-layers following equation (2). Furthermore, formation of nanoscale local BCC and distorted FCC structures (red filled area) can be observed at the intersection site. Similar features have been reported during twin/twin interactions in Au nanowires [26], but seldomly reported for ε-ε interactions in high entropy alloys. For the intersection shown in Fig. 4(f), six interfacial dislocations are observed but without local

change of the thickness of the horizontal band. The result of thin interaction is a new grain boundary identified as $\{10\bar{1}0\}\{1\bar{2}11\}71.3^{o}$ asymmetric boundary.

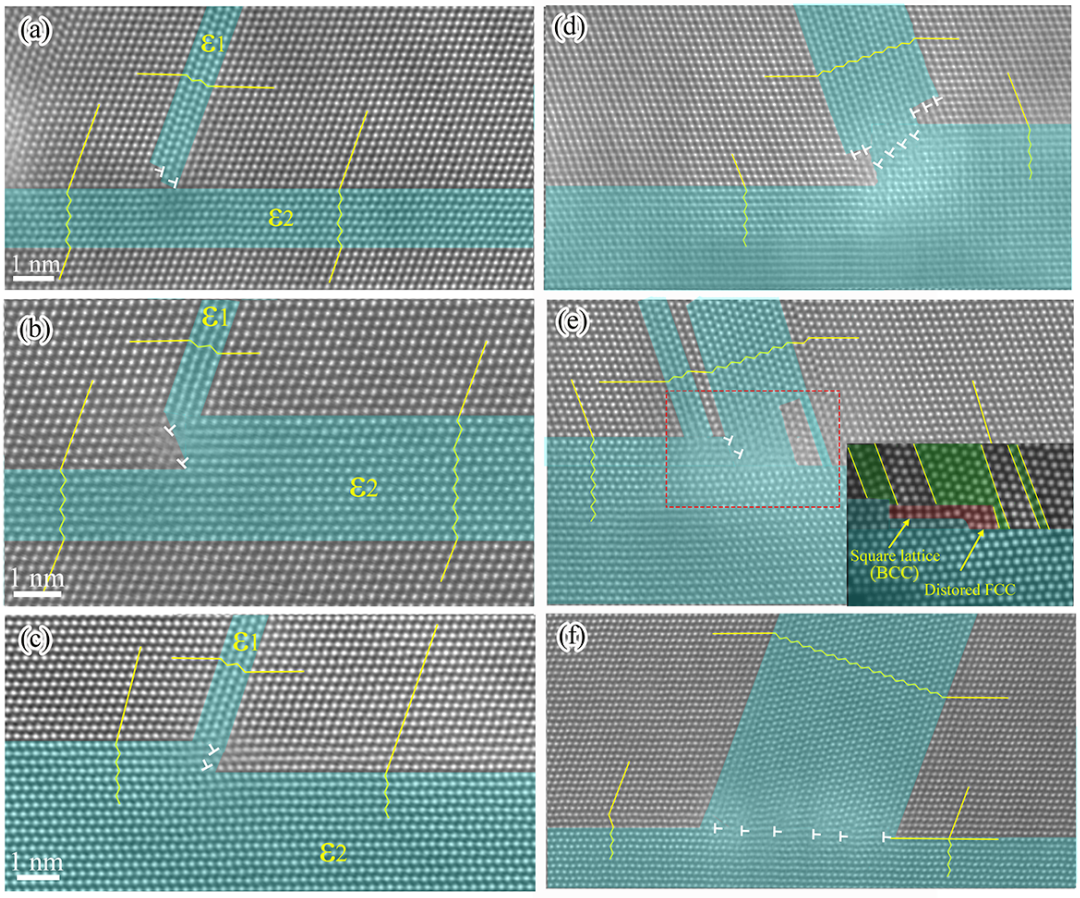

Fig. 4 (a, b, c) Interaction of a 4-layer inclined ε-HCP with thicker primary ε-HCP laminate (viewed along $<110>_{\gamma}$ zone axis). The partials leading the incident bands are blocked at the vicinity of the phase boundary in (a), while the growth of the primary ε-HCP due to the reaction of the incident partials with the phase boundary can be observed in (b) and (c). (d, e, f) Interaction of thicker inclined ε-HCP bands with primary ε-HCP leading to different intersection products. (d) shows partial cross-slip of the inclined ε-HCP, (e and f) show the formation of local BCC, distorted FCC structures and $\{10\bar{1}0\}\{1\bar{2}11\}71.3^{o}$ asymmetric boundary at the intersections.

Fig. 5 shows details on the intersection mechanisms between ε-HCP lamellae with nearly similar thickness. Figs. 5(b, c) exhibit atomic-resolution ABF-STEM micrographs of two intersection regions marked by blue and red dashed squares in the low-magnification micrograph of Fig. 5(a). In Fig. 5(b), the two inclined ε-HCP lamellae (from the upper and bottom sides of the

horizontal ε-HCP band) are blocked at the interface as evidenced by the local increase of strain field, leading to 3° counter-clock rotation of the horizontal ε-HCP laminate at the intersection site. In Fig. 5(c) and enlarged image of Fig. 5(d), the upper ε-HCP band slightly penetrates in the primary ε-HCP, with the edge of upper ε-HCP counter-clock rotated 7° while no orientation change is observed for the primary ε-HCP. These local lattice rotations could be attributed to the increase of local strain at the intersection site.

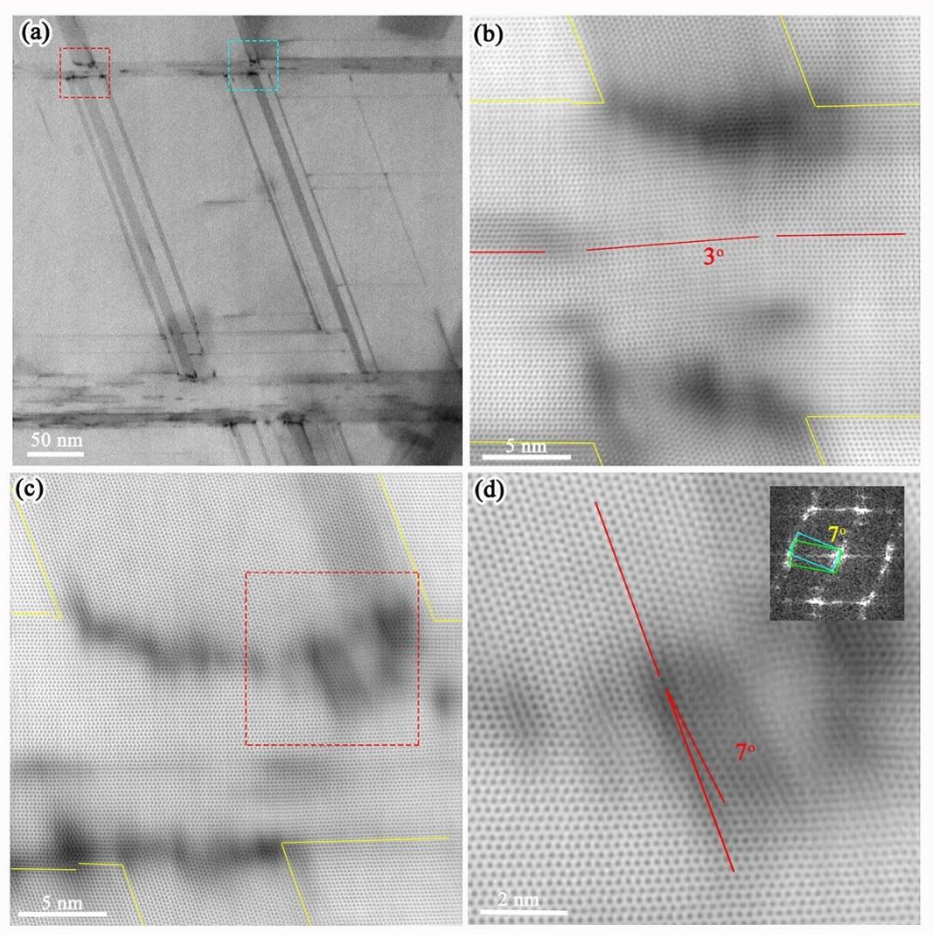

Fig. 5 (a) Low-magnificent <110>$_\gamma$ ABF-STEM micrograph of the ε-ε interaction in sample deformed at ε=0.2, (b, c) HAADF-STEM micrographs of two typical ε-ε interactions marked by red dashed squares in (a), (d) enlarged images of the edge of the interaction region delimited by blue dashed squares in (c) and the corresponding FFT.

For the ε-ε interactions observed in the sample deformed at ε=0.2, most of the inclined ε-HCP lamellae have penetrated through the primary ε-HCP lamellae, resulting in different ε-ε intersection products. Fig. 6 shows BF-TEM micrographs of two typical ε-ε intersection sites observed in this

sample. The inclined ε-HCP laminate rotates by 19.7° when penetrating the primary ε-HCP and then changes back to its initial orientation after crossing the primary ε-HCP (red dashed lines in (a) and (b)). When the inclined ε-HCP has smaller thickness compared with the primary ε-HCP (Fig. 6(a)), the interface of the primary ε-HCP is almost not changed (shown by yellow dashed line). When the inclined ε-HCP has similar thickness as the primary ε-HCP (Fig. 6(b)), both the inclined and primary ε-HCP lamellae are sheared and the intersection region is rigid-body-rotated compared with the two crossing ε-HCP lamellae (blue dashed circles in Fig. 6(b)). Once again, these results confirm that thickness differences between the two crossing ε-HCP play a pivotal role in dictating the nature of the ε-ε intersection products.

Fig. 6(c, e) shows HAADF-STEM micrographs of two different ε-ε intersections. For the ε_1-ε_2 intersection site (marked by a red square in Fig. 6(c)) shown in Fig. 6(d), local rigid-body-rotation of the ε_1 lattice by 19.5° is observed. Furthermore, alternating ε_3 and γ_1 bands were formed within the intersection. This phenomenon has been explained by the cooperative shear associated with the initial two ε-HCP variants, and the corresponding orientation changes can be described as rigid-body rotations [19]. The interface between the intersection products and the ε-HCP variants are generally irregular, without a definite boundary plane. Previous works reported the formation of either γ-FCC or secondary ε-HCP variant in carbon-doped DP-HEA or high interstitial-alloyed austenitic steels [16, 19, 21]. In the present study, the co-existence of ε and γ lamellae at the intersection can be attributed to the incomplete ε→γ transformation. The new γ laminate in the intersection exhibits a misorientation angle of 90° with respect to the γ-FCC matrix, which is similar to the ε-ε intersection reported in high Mn steel [16], but different from the 60° rotation observed in the same DP-HEA alloy system [21]. Fig. 6(f) (orange square in Fig. 6(e)) shows an intersection site with a much more distorted lattice and high local density of dislocations. A $\{10\bar{1}1\}$ ε twin with misorientation angle of 56° is observed within the intersection (blue dashed line in Fig. 6(f)).

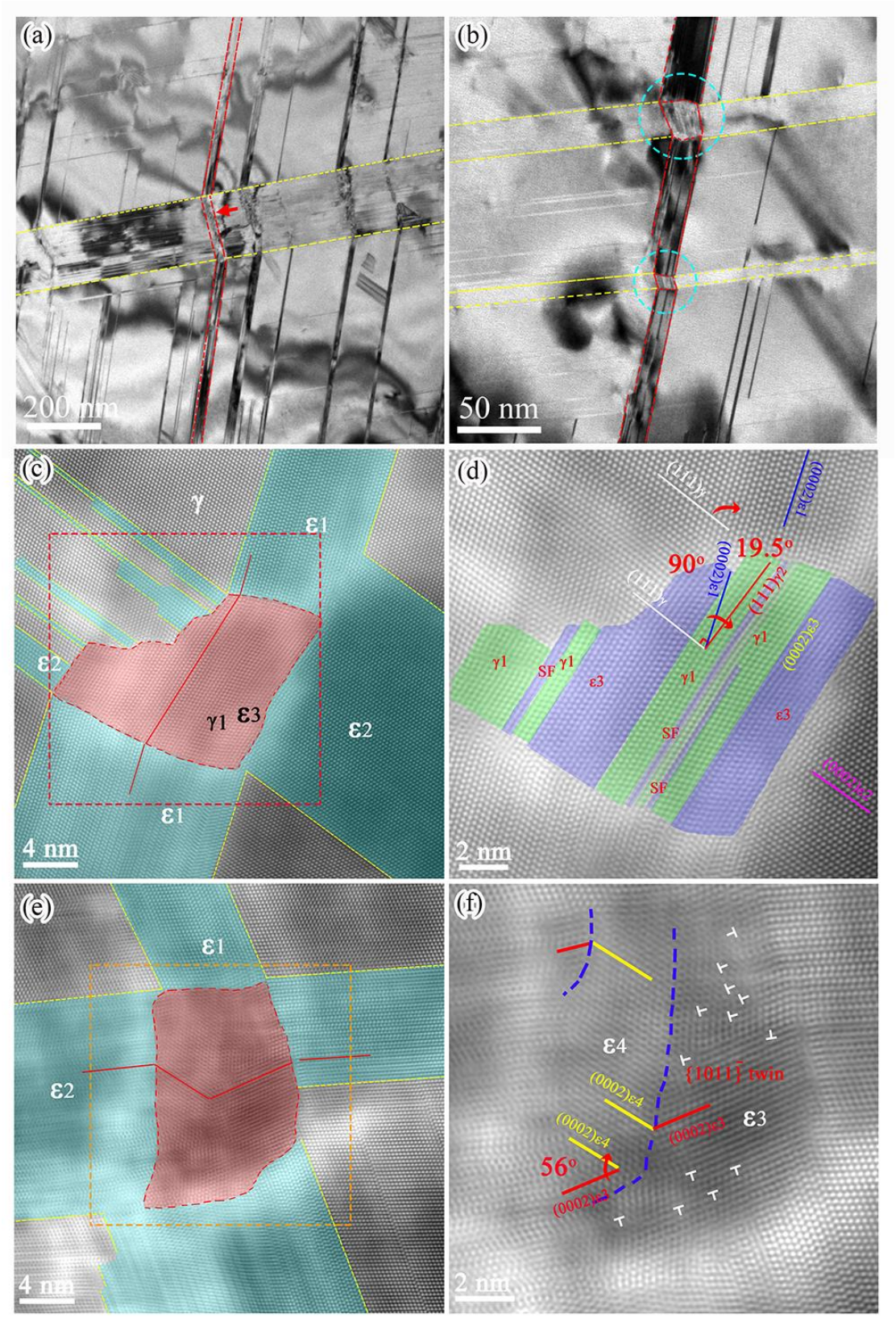

Fig. 6. TEM bright-field micrographs of ε-ε intersection viewed along <110>$_\gamma$ zone axis (a) when the inclined ε-HCP has much smaller thickness compared with the primary ε-HCP, (b) when the two crossing ε-HCP lamellae have similar thickness. The intersections are marked by blue dashed circles,

(c, e) HAADF-STEM micrographs of the two different intersections of two crossing ε-HCP lamellae. (d, f) enlarged images of the intersections marked by red and orange dashed rectangles in (c, e). A $\{10\bar{1}1\}$ ε twin is marked by blue dashed line.

The ε-ε intersections shown in Fig. 7 exhibit significant changes of the morphology of the intersection products. The intersections are more expanded and exceed the area of the two crossing ε-HCP. In Fig. 7(a), a new γ-FCC phase (γ_1) with misorientation angle of 90º with respect to the γ-FCC matrix is observed in the intersection. A new ε-HCP variant (ε_3) is formed close to the reverted FCC phase. It is clear that the ε_3 variant exhibits a quasi-twin misorientation angle of 90º with respect to ε_1 (86º for $\{11\bar{2}0\}$ twin). Similar quasi-twin boundaries have been reported in compressed submicron-sized single-crystal magnesium [27]. Such feature is attributed to the re-arrangement of atoms, which acts as a precursor of the $\{11\bar{2}0\}$ twin. In Fig. 7(b), a secondary ε-HCP (ε_3) is formed at the intersection with rigid-body-rotation by 19.5º relative to ε_1, and 90º rotation relative to ε_2, suggesting a quasi-twin orientation relationship between ε_3 and ε_2. Note the growth of ε_3 which leads to the consumption of the initial ε_1-HCP variant.

Fig. 7(c) shows another intersection of two ε-HCP bands where the new ε-HCP variant (ε_3) consumed a wide part of the initial ε phase (ε_1). Enlarged STEM micrographs of the edge of the new ε-HCP (ε_3) is shown in Fig. 7(d) (yellow rectangle in Fig. 7(c)). In this image, the ε_3 variant exhibits a $\{11\bar{2}0\}$ twin relationship with the initial ε_2, confirming that the quasi-twin boundaries can gradually transform to the $\{11\bar{2}0\}$ TBs during the interaction. The orientation relationship between ε_3 and γ matrix can be identified as $\{11\bar{2}0\}_{\varepsilon}//\{210\}_{\gamma}$, different from the typical Shoji-Nishiyama (S-N) orientation relationship [28]. Fig. 7(e) shows a $\{11\bar{2}0\}$ twin formed within ε_3 (red dashed square in Fig. 7(c)). Note the faceted morphology of this boundary with local deviation from the $\{11\bar{2}0\}$ CTB orientation to high-angle $\{0001\}\|\{10\bar{1}0\}$ basal–prismatic (BP/PB) boundaries [29]. The coexistence of these boundaries leads to twin growth. Moreover, some nano-sized grains (red arrows in Fig. 7(c)) are formed at the twin boundary and within the ε_3-HCP variant. Fig. 7(f) shows enlarged STEM micrograph of the nano-sized grain marked by blue dashed square in Fig. 7(c). The ε_4 variant in the nano-sized grain does not exhibits specific orientation with the adjacent ε variants (63º rotation with respect to the ε_3 variant and 26º rotation with respect to the ε_2 variant).

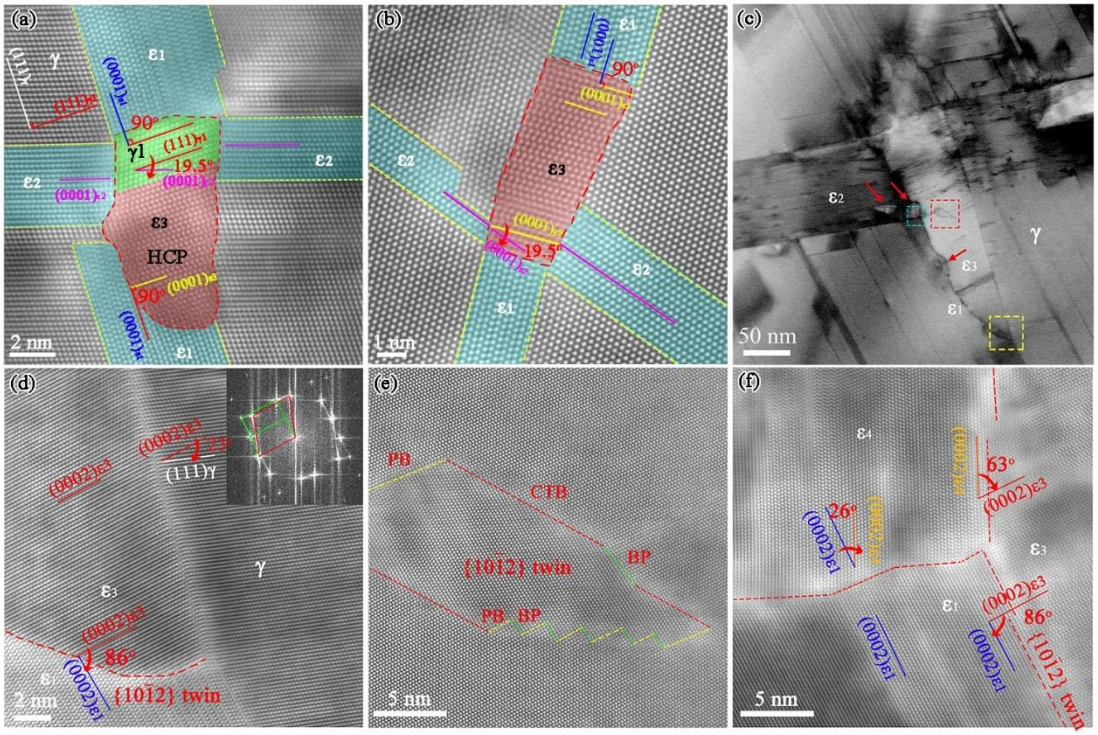

Fig. 7(a, b) <110>$_\gamma$ HAADF-STEM micrographs of two intersections with the activation of ε-twin. (c) Low magnificent <110>$_\gamma$ HAADF-STEM micrograph of an intersection with bigger size. (d, e, f) are enlarged <110>$_\gamma$ STEM micrographs marked by yellow, red and blue rectangles in (c), respectively. $\varepsilon_{3/\gamma}$ interface, {11$\bar{2}$0} twin and nanosized grains formed at the intersection can be observed.

Fig. 8(a) shows that the interaction of ε-HCP lamellae can lead to the formation of nanosized grains without inter-penetration (red arrows). Fig. 8(b) and 8(c) show the formation of a new 6 nm sized ε grain at the intersection site. The new ε_3 product exhibits a {11$\bar{2}$0} twin relationship with the inclined ε_1, which is different from the quasi-twin with misorientation angle of 90º observed at intersection shown in Fig. 8(a). Besides, ε_3 is 16.4º rotated with respect to ε_2, which is different from the 19.5º rotation in Fig. 7(a). Fig. 8(d) and 8(e) show a necklace of nanosized grains with different orientations formed within a primary ε-HCP band. The invading of large amount of HCP lamellae into the primary ε-HCP laminate has led to local orientation changes of the ε-HCP laminate and the formation of nano-sized ε grains. Fig. 8(f) indicates that, all adjacent ε variants do not exhibit twin or quasi-twin relationship. Indeed, the ε_3 variant in grain 1 exhibits 40º rotation with respect to the

ε_2, and 70° rotation with the adjacent ε_1 variant formed in grain 2. This finding suggests that, when nanosized grains are formed at the intersection, the orientation of the grains do not follow the rigid-body-rotation of 19.5° observed at the intersection of two crossing ε-HCP lamellae.

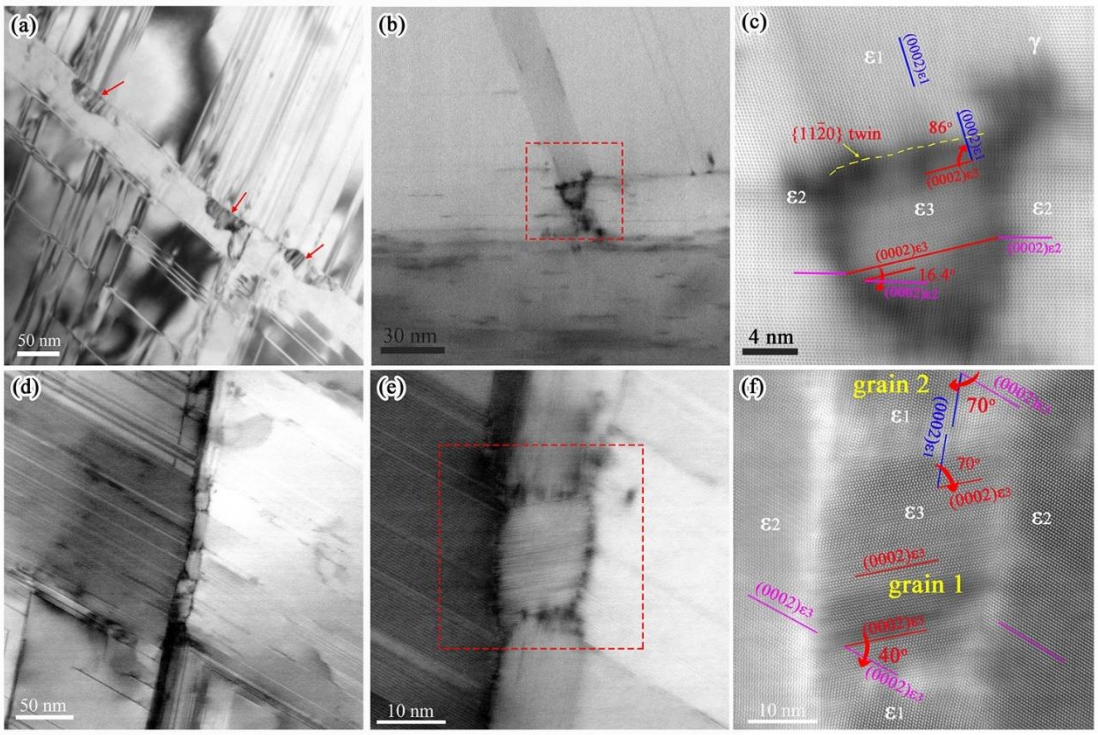

Fig. 8 (a) TEM bright-field micrograph showing the nucleation of nanosized grains at the ε-HCP laminate, (b) the formation of nanosized grain due to the interaction between two HCP lamellae view along <110>$_\gamma$ zone axis, (c) Enlarged <110>$_\gamma$ ABF-STEM micrograph of the nanosized grain, (d) Low magnificent <110>$_\gamma$ ABF-STEM micrograph of the formation of a necklace of nanosized grains in a deformation band, (e, f) enlarged STEM micrographs of the nanosize grains within the same deformation band.

4. MD simulation

Fig. 9 shows two schematics which describe the crystallographic relationship between the two martensite interacting bands. Fig. 9(a) depicts the first mode with a pre-existing ε_1-HCP band connected to a grain boundary. With an increasing applied stress, another ε_2-HCP band is formed and moves towards the pre-existing ε_1. Once ε_2 is contact with ε_1, partial dislocations at the tip of ε_2 are absorbed at the boundary between the two bands. These dislocations will thus dissociate at the boundary leading to the growth or phase transformation of the HCP bands. In Fig. 9(b), instead of

generating a new ε_2 band from another grain boundary, ε_2 nucleates at the connection site of ε_1 and the grain boundary. In this case, ε_1 and ε_2 form a cross structure. The front of ε_2 gradually bows forward, leading to the formation of series of SPDs at the top and bottom boundaries of ε_1. These partials exhibit the same Burgers vector but opposite line direction, attracting each other and facilitating the dissociation of partial dislocations at the phase boundaries. Due to the different distribution of dislocations near the intersection site in the two interaction modes, the local stress state is different, resulting in different dislocation reactions. Molecular statics calculations (shown in supplementary materials Fig. S2) have shown that the SFE in the present alloy equals -84.7mJ/m² in agreement with previous MD results reported by Fang et al. [30]. Next, we will discuss the

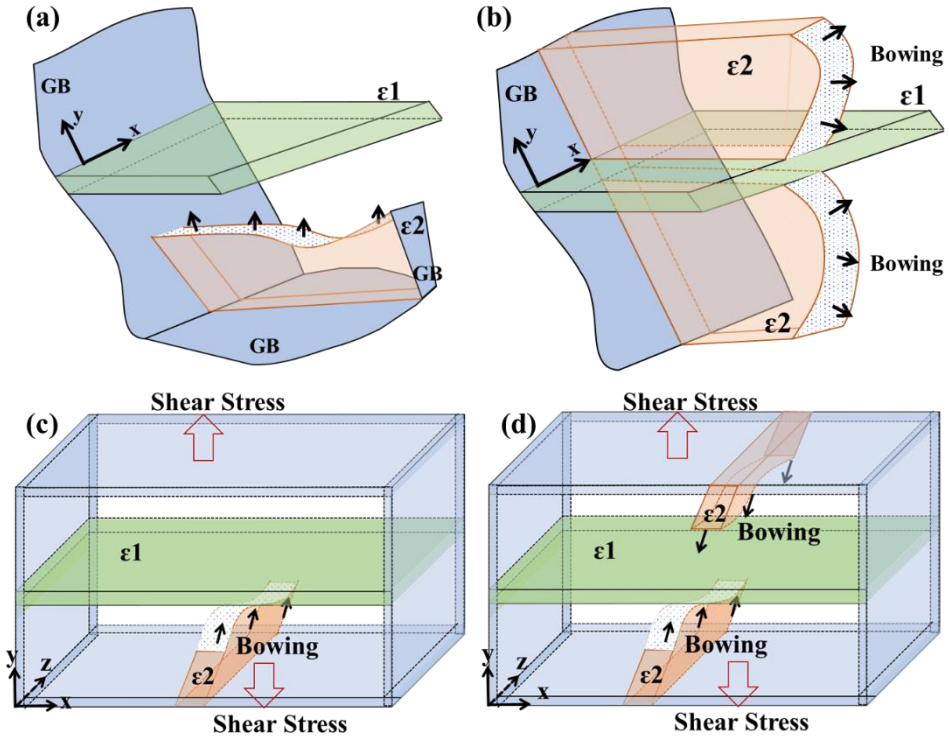

interaction mechanisms of two martensite bands following these two interaction modes through molecular dynamics simulations.

Fig. 9 Schematics of interaction between ε-martensite bands. (a) ε-martensite band expanding towards another ε-martensite band. (b) Interaction between two ε-martensite bands and the formation of a cross shaped structure. (c and d) provide the geometric arrangement shown in (a and b), respectively. The light-blue shaded regions in both Figures (c and d) denote domains subjected to fixed boundary constraints during the simulations.

4.1. HCP interaction mechanisms without penetration

Fig. 10(a) shows the interaction between a pre-existing ε_1-HCP band and a growing ε_2-HCP band. ε_2 expands under the applied shear stress towards ε_1. Fig. 10(b) shows a snapshot of ε_2 reaching ε_1. In this figure, it can be observed that some incoming partial dislocations of ε_2 dissociate far from the interface and form stacking faults on other {111} plane. This indicates that the martensitic bands in the $Fe_{50}Mn_{30}Co_{10}Cr_{10}$ alloy could easily decompose into other slip planes during their propagation, thus interacting with other martensite bands and forming martensite band network as observed in Fig. 2. Fig. 10(c) shows the dissociation of ε_2 on the boundary of ε_1 following the reaction:

$$\frac{1}{6}[\bar{1}1\bar{2}]_{(\bar{1}11)} \rightarrow \frac{1}{6}[\bar{1}2\bar{1}]_{(111)} + \frac{1}{6}[0\bar{1}\bar{1}]_{stair-rod} \qquad (4)$$

Where $\frac{1}{6}[\bar{1}2\bar{1}]_{(111)}$ is SPD gliding in the phase boundary of ε_1, leading to the growth of ε_1 (similar to TEM observations in Fig. 4). With increasing strain, the thickness of ε_1 gradually increases on the right site with gradual absorption of ε_2 into ε_1, see Fig.10(d).

Fig. 10(e-h) shows another reaction where new partial dislocation nucleated at both sides of the $\varepsilon_1/\varepsilon_2$ intersection site. In this case, the ε_2 band was also introduced by the glide of a series of mixed SPDs with Burgers vector of $\frac{1}{6}[\bar{1}1\bar{2}]$. However, an additional shear strain ε_{yx} was used in this case, making the dissociation of SPDs in the X-axis direction possible. The initial stage of interaction between the two martensite bands in Fig. 10(e and f) is similar to what is observed in Fig. 10(a). However, instead of continuous emission of SPDs on one side, other partials are generated in the opposite direction. The dissociation of the first partial dislocation is consistent with equation (4).

As the applied shear stress increases, the $\frac{1}{6}[0\bar{1}\bar{1}]$ stair-rod dislocation dissociates to generate new $\frac{1}{6}[11\bar{2}]_{(111)}$ and $\frac{1}{6}[\bar{1}\bar{2}1]_{(\bar{1}11)}$ partials on the (111) and $(\bar{1}11)$ planes, respectively. The $\frac{1}{6}[11\bar{2}]_{(111)}$ dislocation exhibit opposite screw component compared to $\frac{1}{6}[\bar{1}2\bar{1}]_{(111)}$. They move on opposite directions on the (111) plane under similar resolved shear stress. This process leads to the growth of ε_1 by two atomic layers. The left dislocation $\frac{1}{6}[\bar{1}\bar{2}1]_{(\bar{1}11)}$combines with $\frac{1}{6}[\bar{1}1\bar{2}]_{(\bar{1}11)}$ to form $\frac{1}{6}[\overline{211}]_{(\bar{1}11)}$, while the third incoming $\frac{1}{6}[\bar{1}1\bar{2}]_{(\bar{1}11)}$ partial decomposes again according to equation (4) and enter a new cycle. Each cycle will leave a $\frac{1}{6}[\overline{211}]_{(\bar{1}11)}$ partial at the interface.

Therefore, SPDs nucleate and slip at both side of ε_2. No thickness difference can be found from the two sides of the ε_2.

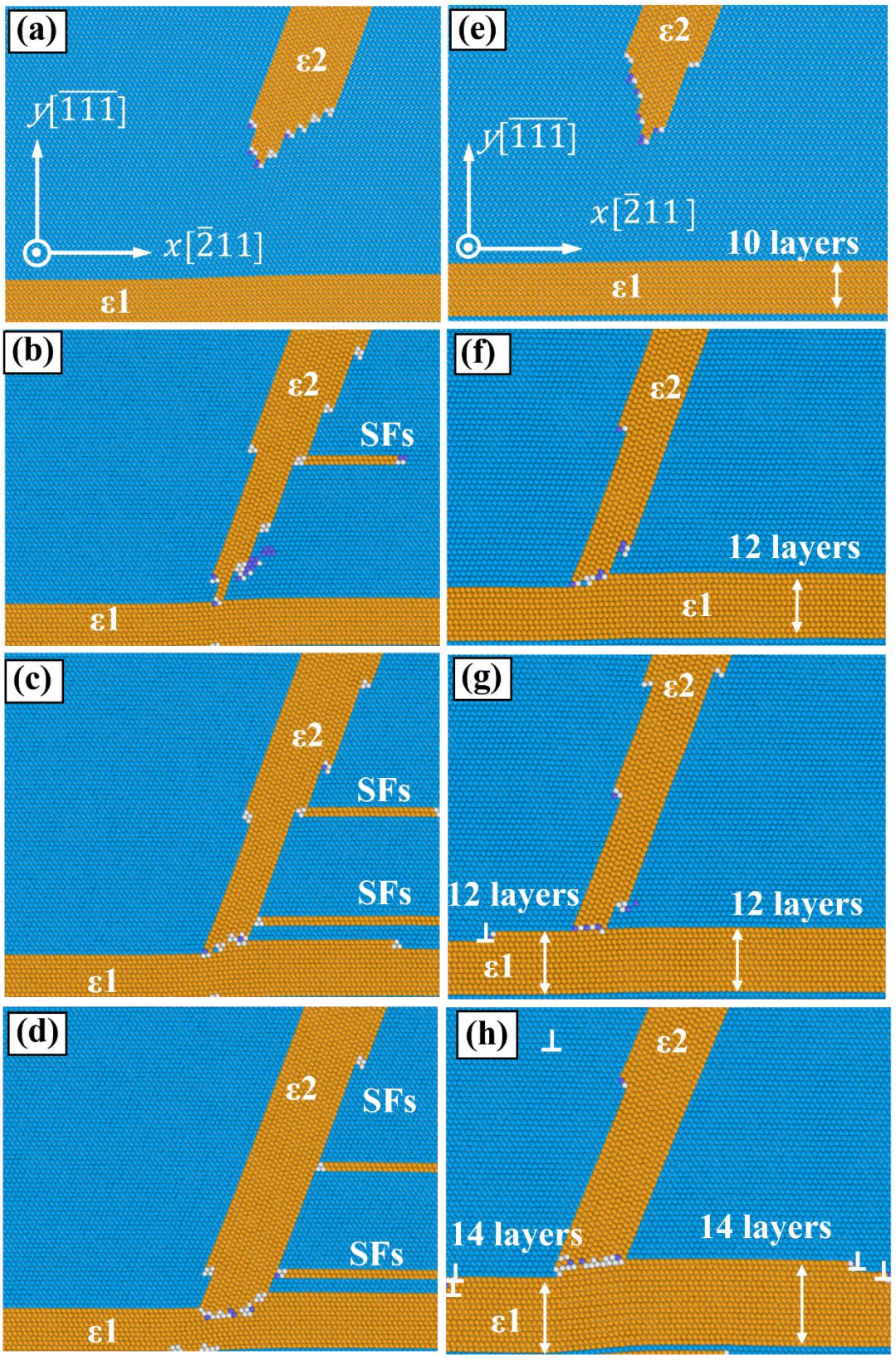

Fig. 10 Interaction between two ε-martensite. (a) Initial atomic configuration. The ε_2 band was

created by the creation of a group of mixed Shockley partial dislocation $\frac{1}{6}[\bar{1}1\bar{2}]$. (b) ε_2 reaches ε_1. (c-d) Dissociation of ε_2 at the boundary of ε_1 leading to the growth of ε_1. (e) Initial atomic configuration. (f) Two martensitic bands intersect, resulting in SPD slip in the acute angle region of the intersection, which subsequently leads to the growth of ε_1. (g) The second SPD nucleated and slip in the obtuse angle region of the intersection, leading to growth of ε_1. (h) The interaction of two martensite bands leads to the continuous growth of ε_1 from 10 to 14 atomic layers.

4.2. HCP interaction mechanisms with penetration

In this section, two types of HCP interaction mechanisms with penetration are investigated, including the formation of quasi-twin in the crossing region and the occurrence of phase transformation. The Burgers vectors of the partial dislocations of martensite are the same in both mechanisms, but different interaction modes could lead to different local structures.

Fig. 11 shows the transmission of a martensite band across another. Fig. 11 (a) shows the relaxed model, containing two martensite bands. In this case, the ε_2 band was introduced by gliding a series of edge SPDs. The partials at the tip of ε_2 move under the applied shear stress towards the ε_1 band where they are blocked by the boundary of ε_1. In this case, a new martensite variant is formed (Fig. 11(b)), while no dissociation of dislocations at the boundary can be observed. The new martensite variant ε_3 (quasi-twin relationship with ε_2) nucleates at the contact site of ε_1 and ε_2, then gradually expands to the right side within ε_1. It also exhibits a quasi-twin relationship with ε_2. The atom displacement map in Fig. 11(e) indicates that the transformation from ε_1 to ε_3 is accomplished by shuffle of atoms within the crossing HCP structure. The lattices of ε_1 and ε_3 are shown in Fig. 11(f), with one HCP embryo parasitizing inside another. The red and blue symbols outline ε_1 and ε_3, respectively. The two structures are rotated 90° relative to one another. Under the applied stress, the blue HCP structure can transform to the red one. The arrows indicate the possible route for the required atomic rearrangements. Such behavior is accompanied by the emission of new SPDs in the FCC matrix on top of ε_1 (Fig. 11(c)), leading to the formation of new HCP band (ε_4 in Fig. 11(d)). Note that ε_3 variant continues its expansion, not only in ε_1, but also in the FCC matrix. This configuration agrees with the TEM observation shown in Fig. 7(b) (i.e. rapid growth of ε_3 band can be well-resolved).

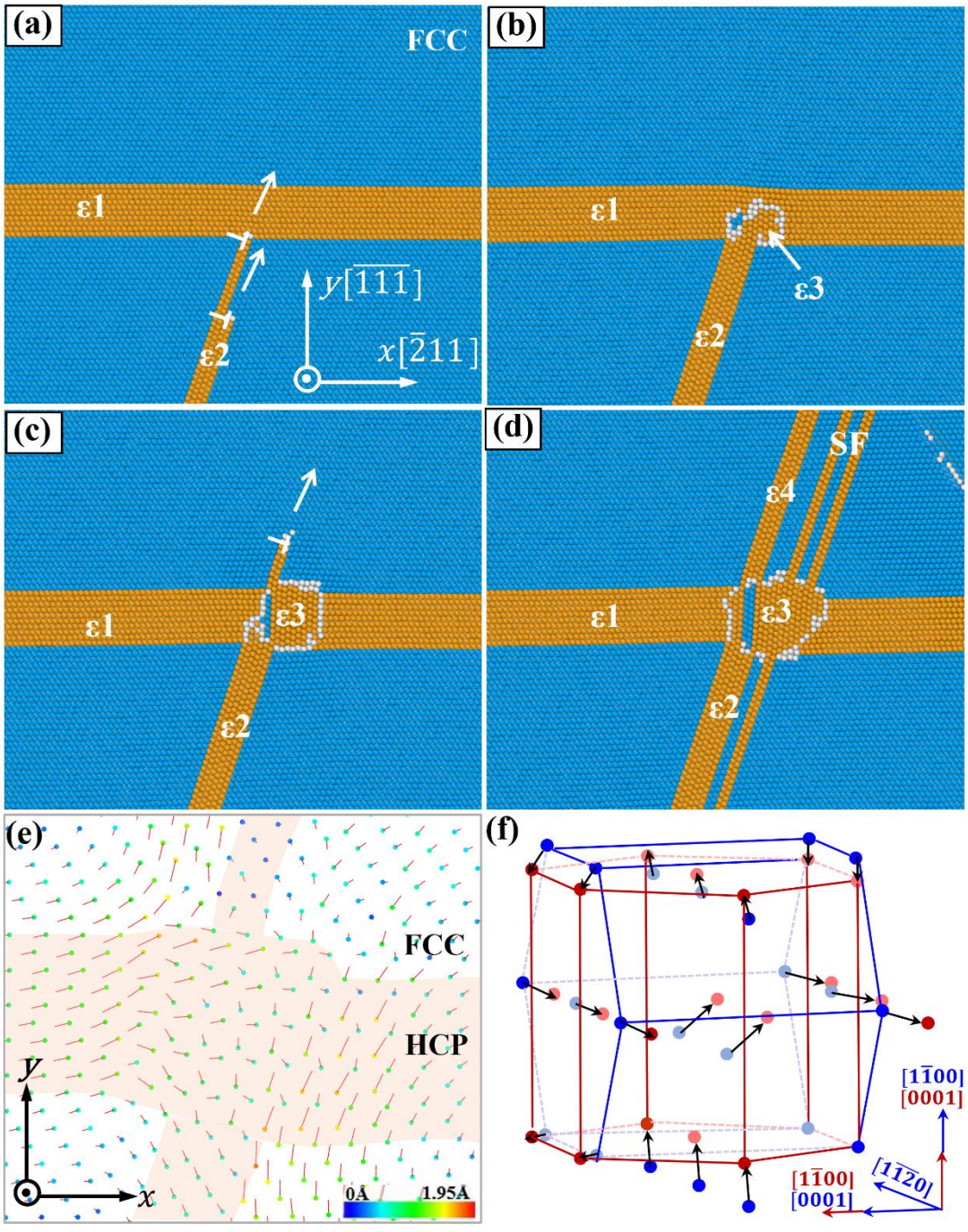

Fig. 11 Transformation for ε-martensite band across another martensite band. (a) The atomic configuration showing the initial state of the model. (b) Snapshot of the early stage of interaction. (c) ε_2 crosses ε_1. (d) Formation of a new martensite variant ε_3 in the intersection site. (e) The relative displacements of atoms at crossing HCP area from snapshot (a) to (d), showing atomic shuffle within the crossing HCP structure. (d) The parent HCP lattice (blue) and quasi-twin HCP lattice (red).

For a martensite band looping another band, the resulting interaction process is very different.

Fig. 12(a) shows the relaxed model containing three martensite bands, where ε_2 in upper and lower part of ε_1 is introduced by gliding series of edge partial dislocations with similar Burgers vector but opposite line direction. When ε_2 interacts with ε_1, several SPDs nucleate and glide from the boundaries of the intersection site towards the opposite boundaries, leading to local phase transformation from HCP to FCC (Fig.12(b)). In Fig.12(c), with increasing deformation, new HCP variant (ε_3) is formed at the boundary of the γ_1-FCC phase. The new ε_3 HCP variant grows within the matrix at the expense of the ε_2 variant with the mission of new SPDs in the FCC matrix (similar to the mechanism shown in Fig. 11).

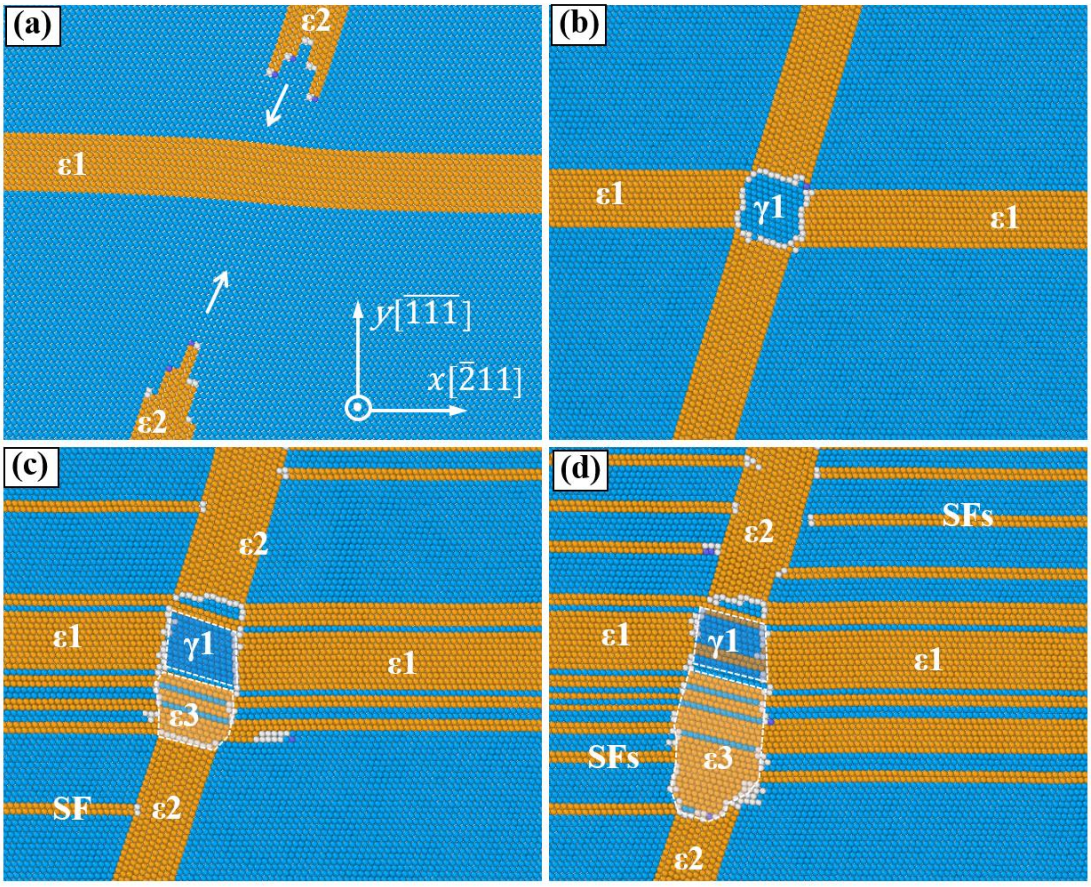

Fig. 12 Bidirectional phase transformation induced by martensite bands interaction. (a) Atomic configuration showing the relaxed model. (b) Snapshot showing the phase transformation from HCP to FCC induced by martensite bands intersection. (c) Snapshot showing the formation of a third martensite variant at the boundary of the FCC phase. (d) Snapshot showing the growth of variant ε_3.

5. Discussion

5.1. Nucleation mechanisms of HCP

In this work, different nucleation mechanisms of ε-HCP phase have been unravelled using high resolution STEM and MD simulations. Before deformation, few annealing ε-HCP martensite and a high density of SFs are formed, indicating a low stacking fault energy. These SFs act as ε-HCP nuclei during deformation. The continuous nucleation of SFs during deformation promotes the nucleation and the growth of new ε-HCP. Previous works in the literature reported that the multiplication and expansion of SFs inside localized microbands is the main mechanism controlling the formation of ε-HCP [31]. Two SFs separated by one atomic layer correspond to a 4-layer ε-HCP. In the present work, two main ε-HCP nucleation mechanisms are evidenced. First, the six-plane mechanism proposed by Mahajan and Chin [10], in which the interaction between co-planar dislocations results in the formation of 6-layer ε-HCP phase (Fig. 3). Secondly, the activation of multiple slip leads to the alternative nucleation and growth of ε-HCP by the stair-rod cross-slip mechanism [9, 32]. When the incoming dissociated dislocations glide towards the ISF or ε-HCP nuclei, the leading partial can dissociate into a stair-rod sessile dislocation and new SPD forming one atomic layer above the ISF and transforming the ISF to a 4-layer ε-HCP (Fig. 3). The same mechanism is observed when SPD interacts with pre-existing HCP laminate leading to the growth of the ε-HCP phase by two layers. The simultaneous activation of multiple nucleation mechanisms of ε-HCP phase in the $Fe_{50}Mn_{30}Co_{10}Cr_{10}$ HEA enables the formation of a high density of ε-HCP thin lamella during deformation, enhancing the strain hardening capacity of this alloy.

5.2. Interaction mechanisms between HCP variants

Various mechanisms are involved in the interaction processes between two conjugated ε lamellae. The selection of a specific intersection product is dictated by the thermodynamic stability of the competing phases and the amount of stress produced by the incident plate. The thermodynamic stability of the competing phases depends on the chemical composition of the alloy [33]. In shape memory alloys, stainless steels and high Mn- steel, the formation of the α′ martensite occurs at the intersection of two crossing ε-HCP martensite lamellas, which is associated with two-step γ→ε→α′ transformation or direct γ→α′ transformation [17, 34, 35]. In the Fe-30Mn-4Si-2Al TRIP/TWIP steel investigated by Zhang et al. [16, 18], a γ phase rotated by 90° relative to the matrix

is generated at the intersection without any α′ or secondary ε. In the present study, no α′ martensite is observed at the intersection sites. This can be attributed to the higher driving force required to form α′ in DP-HEA. The stress amount produced by the incident plate depends on the thickness difference between the two interacting ε lamellae, deformation levels and crystal orientation. The orientation dependence of the ε intersection reactions has been well-resolved in previous literature [18], which is not the main focus of the present work. The deformation level defines the stress imposed to the incoming inclined ε-HCP, and thus the ability of this ε-HCP to penetrate the primary ε-HCP or not. The thickness of the inclined ε-HCP determines the number of the leading partials and thus the shear imposed on the primary ε-HCP.

Under low deformation level, the inclined ε-HCP can hardly penetrate into the primary ε-HCP laminate. Two main reactions are revealed: (i) The inclined ε-HCP is blocked with the leading partials accumulating at the interface of the primary ε-HCP and no thickness variation of the two variants; (ii) The leading partials of the inclined ε-HCP dissociate and cross-slip into the n+2 plane above the primary ε-HCP boundary, leading to the growth of the primary ε-HCP by two {111} planes. At the end of this process, the thickness of the primary ε-HCP is equal to the thickness of the inclined ε-HCP. In most cases, the two mechanisms coexist and the thickness of the primary ε-HCP remains usually smaller than the thickness of the inclined ε-HCP. When the inclined ε-HCP has much smaller thickness compared the primary ε-HCP, the orientation of the primary ε-HCP is hardly affected by interaction due to the small stress involved. When the inclined ε-HCP has a thickness similar to the primary ε-HCP, the inclined ε-HCP is blocked by the primary ε-HCP. In this case, the partial dislocations at the tip of the inclined ε-HCP accumulates at the boundary of the primary ε-HCP, leading to local rotation of the inclined ε-HCP (about 3°-6°) in order to accommodate the increase of the local interfacial strain. In addition, distorted FCC structure and local BCC structure are also formed in some intersections due to the high stress involved.

The present work demonstrates in some cases (experimental result of Fig. 4(f) and simulated result of Fig. 10(h)) that the emitted partial dislocations can glide to both the left and right side of the primary HCP during the intersection, resulting in similar HCP growth along both sides of the intersection site. This phenomenon is less frequent than the HCP band growth at one side of the intersection region. Such behavior can be explained by analyzing the energy barrier of the dislocation reactions. Based on the crystallographic relationship between martensitic bands, when

the inclined ε-HCP interacts with the primary ε-HCP, the partial dislocations at the tip of the inclined ε-HCP can only be 90° edge or 30° mixed Shockley partials. It is difficult for these two types of dislocations to directly cross the interfaces of various discontinuous slip systems.

Therefore, it is more common to dissociate at the interface into a 30° partial and a sessile partial dislocation at the interface. The energy barrier of the reaction process can be calculated by the change in dislocation energy. According to the elastic dislocation energy per unit dislocation line length, the energy barrier for a 30° partial dissociating into a 30° partial and a stair rod dislocation (for instance, the examples in Fig.11-12) can be calculated as:

$$\triangle E_1 = \frac{Ga^2}{72\pi(1-\nu)} ln\frac{\sqrt{2}d}{a} + \frac{Ga^2}{72\pi(1-\nu)} ln3a \qquad (5)$$

where β is the angle between the Burgers vector and the dislocation line, G is the shear modulus, ν is the Poisson's ratio, d is grain size, and a can be calculated as

$$\frac{\sqrt{3}e^{1+\frac{1-2\nu}{4(1-\nu)}(1-\nu)}}{\sqrt{2}[sin^2\beta + e^{\frac{1-2\nu}{4(1-\nu)}(1-\nu)cos^2\beta}]} \qquad (6)$$

The sessile stair-rod dislocation can dissociate again to form two 30° partials as depicted in Fig.10(h). The energy barrier for this process can be written as:

$$\triangle E_2 = \frac{Ga^2(10-9\nu)}{144\pi(1-\nu)} ln\frac{\sqrt{2}d}{a} + 5.5\frac{GA^2}{72\pi(1-\nu)} \qquad (7)$$

The comparison of $\triangle E_1$ and $\triangle E_2$ shows that $\triangle E_2$ is much higher than $\triangle E_1$, indicating that the case in Fig.10(e-h) is less energetically favorable than the case shown in Fig.10(a-d). This could explain why in most of TEM observations, the martensite band grows to one side of the intersection region. The 90° partial is not considered because it cannot directly dissociate into partial dislocations at the phase boundary (no screw component).

Under high deformation levels, the inclined ε-HCP can be transmitted across the primary ε-HCP. When the inclined ε-HCP exhibits much smaller thickness compared to the primary ε-HCP, the inclined ε-HCP can penetrate through the primary ε-HCP without affecting its orientation. When the two crossing ε-HCP bands have similar thickness, rigid-body-rotation occurs at the intersection. In this case, the formation of secondary ε-HCP as well as reverse transformation from ε-HCP to γ-FCC are both observed at the intersection site. The secondary γ at the intersection exhibits a misorientation of 90° with respect to the γ matrix, while the secondary ε exhibits rigid-body-rotation of 19.5° and 90° with respect to the two crossing ε-HCP lamellae, suggesting a quasi {11-20} twin

relationship with one of the initial ε-HCP. The formation of these ε quasi-twins consumes the initial ε and thus contributes to the accommodation of the local strain at the intersections. As a result, the interfaces between various secondary variants are sometimes "wandering" and appear boundaryless or larger than the two variants. The quasi-twin can gradually transform to $\{11\bar{2}0\}$ twin during the growth of secondary ε as shown in Fig. 7(c). Besides, some nano-sized grains can also form at the intersection. These grains do not necessary exhibit a twin relationship with each other. The formation of secondary γ and secondary ε phases can be explained by the intersecting-shear mechanism proposed by Yang and Wayman [15]. The γ→ε transformation occurs by the glide of SPDs on every second (111) plane with shear angle of 19.5° [20, 36]. In the intersecting-shear mechanism, the γ→ε transformation is decomposed into two steps of the half-twining shear T/2 and subsequent shuffling [15]. The interaction of two ε lamellas can be regarded as undergoing double T/2 shear on two conjugate shear systems. The original FCC stacking recovers after the double shear, with rotation of γ by 90° relative to the matrix. In other words, the interaction of two ε lamellae, if they are visualized as two intersecting T/2 shears on conjugate shear systems of FCC lattice, leads to rigid-body-rotation of the FCC variant and the formation of secondary γ variant [16]. The formation of secondary ε variants is now considered as a result of the secondary γ variant if the γ→ε shear process (i.e. the inhomogeneous T/2 shear) occurs in the secondary γ variant. Since the secondary γ phases are usually surrounded by the initial ε lamellas, it is energetically favorable for γ to transform to secondary ε variants. In the present work, both of secondary γ and secondary ε coexist in the intersection region, which is probably caused by reverse transformation between γ and ε. Fig. 13 summarizes the different ε-ε intersection products shown in the present work.

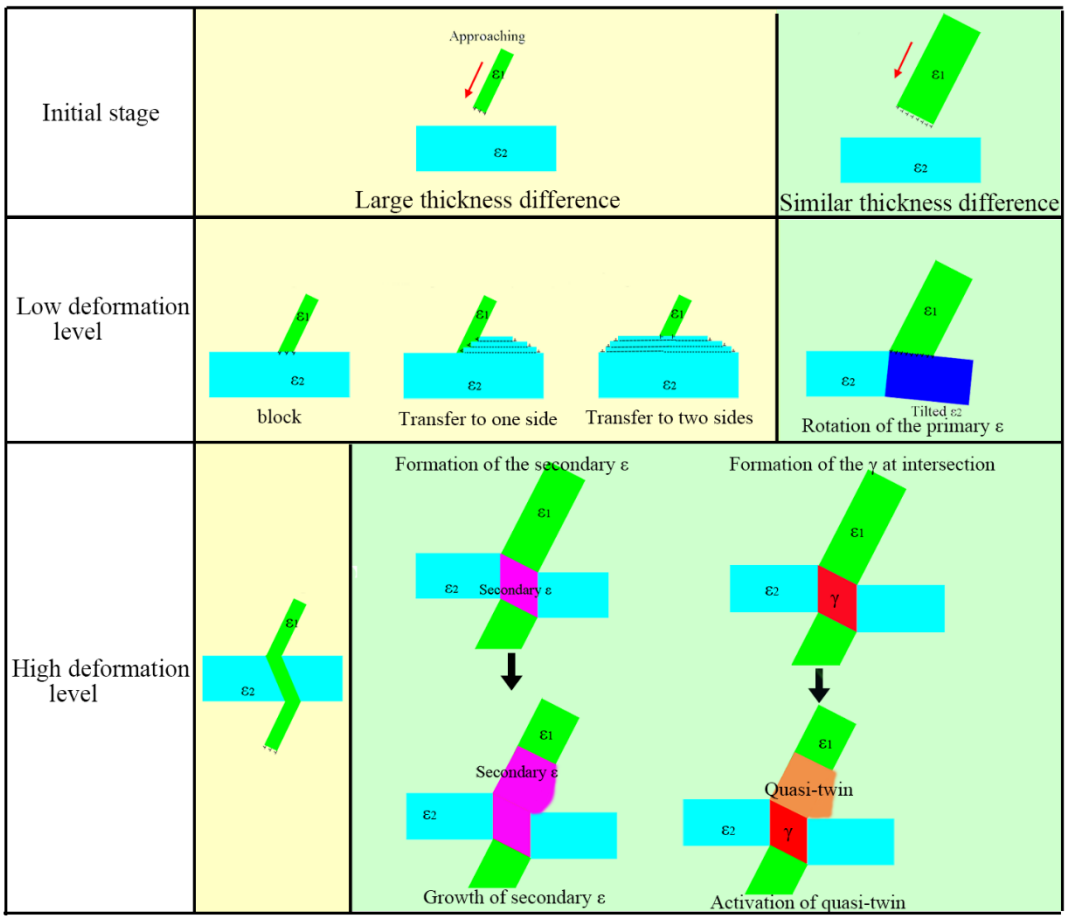

Fig. 13. Schematic illustration of different ε-ε intersection products under different deformation levels and thickness differences between two crossing ε variants.

The high strain hardening capacity of the investigated HEA can be directly associated to the progressive nucleation of a high density of HCP lamellae. This is a direct result of activation of transformation-induced plasticity (TRIP) due to the formation of a harder phase, with new interfaces, and to the generation of extra dislocations in the surroundings of the transformed lamella. More precisely, the first contribution is the progressive generation of hard domains (ε-HCP lamellae) that will carry load through elastic deformation. The ε-HCP lamellae are hard owing to the small size but also due to the limited number of slip systems. This means that all along the deformation process, new hard domains are generated that raise the load carrying capacity maintaining a high strain hardening capacity. It is important that the transformation be progressive same as for TRIP assisted multiphase steels [37, 38] in order to keep the high strain hardening at large strains hence a good uniform elongation. The second important effect is the continuous generation of hard interfaces that

block the intersecting ε-HCP lamellae (Fig. 13). This is another contribution similar to TWIP steels [32, 39, 40]. As a third contribution, the transformation of the ε-HCP lamellae is accommodated by the generation of extra partial dislocations that can then carry the plastic deformation and contribute to strain hardening. The relative importance of these three contributions is difficult to quantify without deeper micromechanical analysis [41], that goes out of the scope of the present study.

Strain hardening conditions the resistance to plastic localization, but a second "ductility" indicator is the resistance to damage and final fracture. The detailed characterization performed in this work also indicates the activation of some mechanisms that can potentially relax the stress concentrations and delay the occurrence of damage at "hot spots". Indeed, the reverse transformation acts here as a self-accommodation mechanism which can better redistribute lattice defect arrangements in damage-critical regions where the local stresses could reach very high levels [5]. Furthermore, the ε-ε intersection can promote the activation of $\{11\bar{2}0\}$ twins or quasi $\{11\bar{2}0\}$ twin near the intersection. These nanosized twins can accommodate the stress concentration at the intersection and thus contribute as an extra source of work hardening. In summary, the HCP nucleation and intersection mechanisms explored in the present work shed new light on the origin of the remarkable strain hardening capacity of the TRIP-assisted high-entropy alloys, steels and shape memory alloys with similar stacking fault energy (SFE) while potentially mitigating the occurrence of premature damage.

5. Conclusion

The present work focuses on detailed investigation of the nucleation and intersection mechanisms of ε-HCP in a $Fe_{50}Mn_{30}Co_{10}Cr_{10}$ high entropy alloy. The results can be summarized as follow:

1. The six-plane and stair-rod cross-slip mechanisms are responsible for the nucleation of ε-HCP in the DP-HEA alloy. The presence of high density of stacking faults (SFs) in the as-annealed sample act as nuclei for stress-induced ε-HCP. The simultaneous activation of multiple nucleation mechanisms of ε-HCP phase enables the formation of a high density of ε-HCP thin lamella during deformation.

2. Various mechanisms are involved in the interaction process between two conjugated ε lamellae. These mechanisms are highly dependent on the deformation level and the thickness difference between the two crossing ε-HCP. Under low deformation level, the thin incoming ε-HCP can hardly

penetrate to the primary ε-HCP laminate. Two reactions are observed: (i) The incoming ε-HCP is blocked with the leading partials accumulating at the interface of the primary ε-HCP; (ii) The leading partials of the inclined ε-HCP dissociate and cross-slip to the n+2 plane above the primary ε-HCP boundary, leading to the growth of the primary ε-HCP by two {111} planes.

3. Regarding the ε-ε interaction mechanisms without penetration, the orientation of the primary ε-HCP is hardly affected by interaction when the inclined ε-HCP has much smaller thickness compared the primary ε-HCP. When the inclined ε-HCP has similar thickness as the primary ε-HCP, the partial dislocations accumulate at the primary ε-HCP boundary, leading to local rotation of the inclined ε-HCP (about 3°-6°). In some case, the emitted partial dislocations can glide to both the left and right sides of the primary HCP during the intersection, resulting in symmetrical growth at the two sides of the intersection site.

4. Under high deformation levels, the inclined ε-HCP can cross the primary ε-HCP. The formation of secondary ε-HCP and reverse transformation from ε-HCP to γ-FCC are two products formed at the intersection. The secondary γ at the intersection exhibits a quasi $\{11\bar{2}0\}$ twin relationship between one of the initial ε. These ε quasi-twins can gradually transform to $\{11\bar{2}0\}$ twin during subsequent transformation. Besides, extensive ε-ε interaction can also lead to the formation of nanosized grains within the band, which do not necessarily exhibit twin relationship with each other.

5. The progressive transformation of ε-HCP lamellae and the ε-ε intersections are expected to significantly increases the work hardening of the DP-HEA due to: (i) the generation of a hard phase and strong interface playing the role of obstacles to dislocation and ε-HCP lamellae, (ii) bidirectional transformation of γ→ε at the intersection, (iii) the activation of $\{11\bar{2}0\}$ twins or quasi $\{11\bar{2}0\}$ twin near the intersection, which accommodate the stress concentration at the intersection, (iv) the formation of nano-sized grains in the alloy.

Acknowledgments

This work was supported by the National Natural Science Foundation of China (Grant No. 52371111, 52471136), the Natural Science Foundation of Jiangsu Province (BK20232025). H. Idrissi is mandated by the Belgian National Fund for Scientific Research (FSR-FNRS).

Competing Interest Statement

Authors declare that they have no competing interests.

Appendix

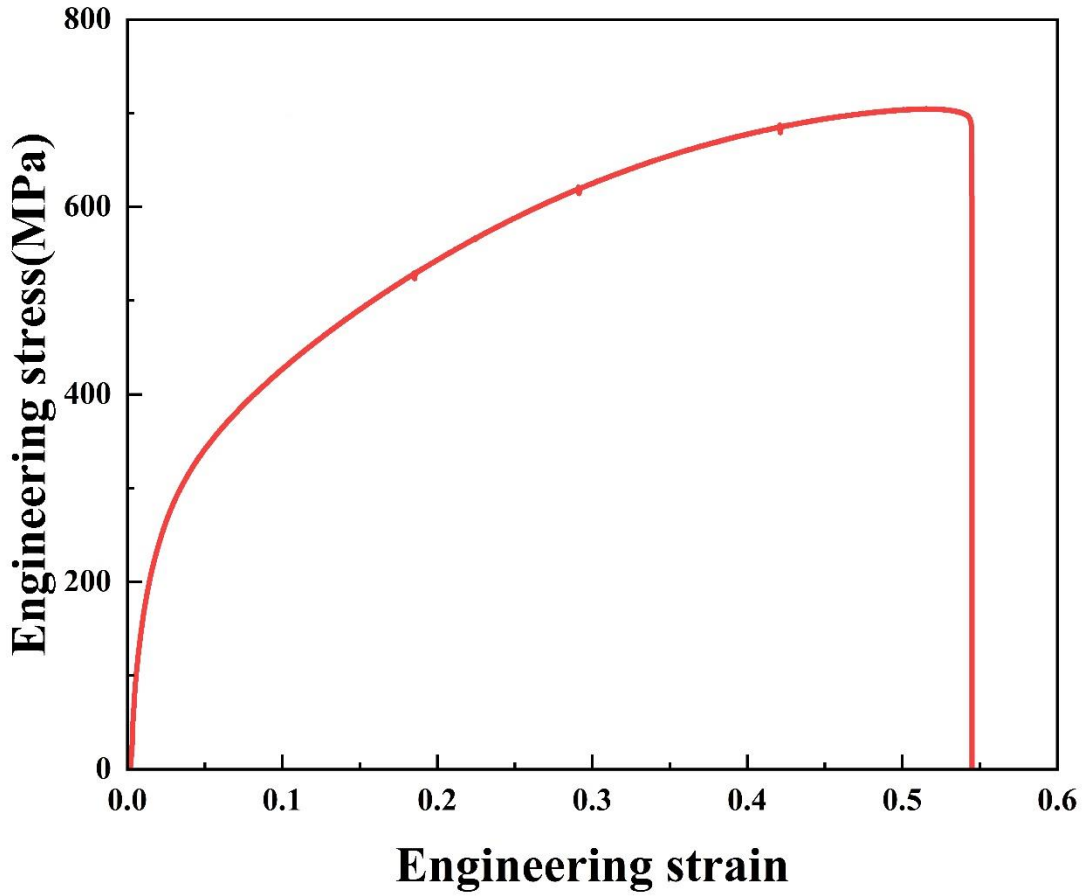

Fig. 14 True stress- true strain curves of the investigated samples

Reference

[1] E.P. George, D. Raabe, R.O. Ritchie, High-entropy alloys, Nat. Rev. Mater. 4 (2019) 515-534.

[2] Z. Li, S. Zhao, R.O. Ritchie, M.A. Meyers, Mechanical properties of high-entropy alloys with emphasis on face-centered cubic alloys, Prog. Mater. Sci. 102 (2019) 296-345.

[3] Z. Li, K.G. Pradeep, Y. Deng, D. Raabe, C.C. Tasan, Metastable high-entropy dual-phase alloys overcome the strength-ductility trade-off, Nature 534 (2016) 227-30.

[4] Z. Li, C.C. Tasan, K.G. Pradeep, D. Raabe, A TRIP-assisted dual-phase high-entropy alloy: Grain size and phase fraction effects on deformation behavior, Acta Mater. 131 (2017) 323-335.

[5] W. Lu, C.H. Liebscher, G. Dehm, D. Raabe, Z. Li, Bidirectional Transformation Enables Hierarchical Nanolaminate Dual-Phase High-Entropy Alloys, Adv. Mater. 30 (2018) 1804727.

[6] Y. Bu, Z. Li, J. Liu, H. Wang, D. Raabe, W. Yang, Nonbasal Slip Systems Enable a Strong and Ductile Hexagonal-Close-Packed High-Entropy Phase, Phys. Rev. Let. 122 (2019) 075502.

[7] T.-H. Lee, S.-D. Kim, H.-Y. Ha, J.H. Jang, J. Moon, J.-Y. Kang, C.-H. Lee, S.-J. Park, W. Woo, J.-H. Shin, J.-W. Lee, D.-W. Suh, H.-U. Hong, Screw dislocation driven martensitic nucleation: A step toward consilience of deformation scenario in fcc materials, Acta Mater.174 (2019) 342-350.

[8] J.A. Venables, The martensite transformation in stainless steel, Philo. Mag. 7 (1962) 35-44.

[9] H. Fujita, S. Ueda, Stacking faults and f.c.c. (γ) → h.c.p. (ϵ) transformation in 18/8-type stainless steel, Acta Metall. 20 (1972) 759-767.

[10] S.Mahajan, M.L.Green, D.Brasen, A model for the fcc-hcp transformation, its application and experimental evidence, Metall. Trans. A 8 (1976) 283-283.

[11] D.T. Pierce, J.A. Jimenez, J. Bentley, D. Raabe, C. Oskay, J.E. Wittig, The influence of manganese content on the stacking fault and austenite/epsilon-martensite interfacial energies in Fe-Mn-(Al-Si) steels investigated by experiment and theory, Acta Mater. 68 (2014) 238-253.

[12] Y.F. Shen, X.X. Li, X. Sun, Y.D. Wang, L. Zuo, Twinning and martensite in a 304 austenitic stainless steel, Mater. Sci. Eng. A 552 (2012) 514-522.

[13] M. Wang, Z. Li, D. Raabe, In-situ SEM observation of phase transformation and twinning mechanisms in an interstitial high-entropy alloy, Acta Mater. 147 (2018) 236-246.

[14] Z. Wang, W. Lu, D. Raabe, Z. Li, On the mechanism of extraordinary strain hardening in an interstitial high-entropy alloy under cryogenic conditions, J Alloy Comp. 781 (2019) 734-743.

[15] J.H.Yang, C.W. Wayman, Intersecting-shear mechanisms for the formation of secondary ε martensite variants, Acta Mater.40 (1992) 2025-2031.

[16] X. Zhang, T. Sawaguchi, K. Ogawa, F. Yin, X. Zhao, A structure created by intersecting ϵ martensite variant plates in a high-manganese steel, Phil. Mag. 91 (2011) 4410-4426.

[17] F. Yoshinaka, T. Sawaguchi, S. Takamori, S. Emura, Transformation-induced plasticity via γ → ε → α' and γ → ε → γ martensitic transformations in Fe–15Mn–10Cr–8Ni–4Si alloy, Mater. Sci. Eng. A 833 (2022) 142583.

[18] X. Zhang, T. Sawaguchi, K. Ogawa, F. Yin, X. Zhao, Orientation dependence of variant selection and intersection reactions ofϵmartensite in a high-manganese austenitic steel, Phil. Mag. Lett. 91 (2011) 563-571.

[19] J.H.Yang, C.W. Wayman, On secondary variants formed at intersections of ε martensite variants,

Acta Mater. 40 (1992) 2011-2023.

[20] T.-H. Lee, H.-Y. Ha, J.-Y. Kang, J. Moon, C.-H. Lee, S.-J. Park, An intersecting-shear model for strain-induced martensitic transformation, Acta Mater. 61 (2013) 7399-7410.

[21] J. Su, X. Wu, D. Raabe, Z. Li, Deformation-driven bidirectional transformation promotes bulk nanostructure formation in a metastable interstitial high entropy alloy, Acta Mater. 167 (2019) 23-39.

[22] W.-M. Choi, Y.H. Jo, S.S. Sohn, S. Lee, B.-J. Lee, Understanding the physical metallurgy of the CoCrFeMnNi high-entropy alloy: an atomistic simulation study, Npj Comp.Mater. 4 (2018) 1.

[23] A. Stukowski, Visualization and analysis of atomistic simulation data with OVITO–the Open Visualization Tool, Model Simul. Mater. Sc. 18 (2010) 015012.

[24] S. Plimpton, Fast Parallel Algorithms for Short-Range Molecular Dynamics, J Comp. Phys. 117 (1995) 1-19.

[25] J.M. How, U. Dahmen, R. Gronsk, Atomic mechanisms of precipitate plate growth, Phil. Mag. A 56 (1987) 31-61.

[26] S. Zhao, Q. Zhu, X. An, H. Wei, K. Song, S.X. Mao, J. Wang, In situ atomistic observation of the deformation mechanism of Au nanowires with twin–twin intersection, J Mater.Sci.Technol. 53 (2020) 118-125.

[27] B.Y. Liu, J. Wang, B. Li, L. Lu, X.Y. Zhang, Z.W. Shan, J. Li, C.L. Jia, J. Sun, E. Ma, Twinning-like lattice reorientation without a crystallographic twinning plane, Nat. Commun.5 (2014) 3297.

[28] C.E. Slone, S. Chakraborty, J. Miao, E.P. George, M.J. Mills, S.R. Niezgoda, Influence of deformation induced nanoscale twinning and FCC-HCP transformation on hardening and texture development in medium-entropy CrCoNi alloy, Acta Mater. 158 (2018) 38-52.

[29] Q. Sun, X.Y. Zhang, Y. Ren, J. Tu, Q. Liu, Interfacial structure of $\{10\bar{1}2\}$ twin tip in deformed magnesium alloy, Scr. Mater.90-91 (2014) 41-44.

[30] Q. Fang, Y. Chen, J. Li, C. Jiang, B. Liu, Y. Liu, P.K. Liaw, Probing the phase transformation and dislocation evolution in dual-phase high-entropy alloys, Int. J Plasticity 114 (2019) 161-173.

[31] L. Ding, A. Hilhorst, H. Idrissi, P.J. Jacques, Potential TRIP/TWIP coupled effects in equiatomic CrCoNi medium-entropy alloy, Acta Mater. 234 (2022) 118049.

[32] H. Idrissi, K. Renard, D. Schryvers, P.J. Jacques, TEM investigation of the formation mechanism of deformation twins in Fe-Mn-Si-Al TWIP steels, Phil. Mag.93 (2013) 4378-4391.

[33] T.-H. Lee, E. Shin, C.-S. Oh, H.-Y. Ha, S.-J. Kim, Correlation between stacking fault energy and

deformation microstructure in high-interstitial-alloyed austenitic steels, Acta Mater. 58 (2010) 3173-3186.

[34] X.-S. Yang, S. Sun, T.-Y. Zhang, The mechanism of bcc α′ nucleation in single hcp ε laths in the fcc γ → hcp ε → bcc α′ martensitic phase transformation, Acta Mater. 95 (2015) 264-273.

[35] J.-B. Seol, J.E. Jung, Y.W. Jang, C.G. Park, Influence of carbon content on the microstructure, martensitic transformation and mechanical properties in austenite/ε-martensite dual-phase Fe–Mn–C steels, Acta Mater. 61(2013) 558-578.

[36] D. Singh, A. Singh, T. Sawaguchi, Elucidating deformation pathways and interface characteristic of self-accommodated dual γ/ε phase microstructure in Fe–Mn–Si–Al alloy, Mater. Charact. 207 (2024) 113521.

[37] L. Delannay, P. Jacques, T. Pardoen, Modelling of the plastic flow of trip-aided multiphase steel based on an incremental mean-field approach, Int. J Solids Struct. 45 (2008) 1825-1843.

[38] M.K. Hatami, T. Pardoen, G. Lacroix, P. Berke, P.J. Jacques, T.J. Massart, Towards ultra-high ductility TRIP-assisted multiphase steels controlled by strain gradient plasticity effects, J Mech. Phys. Solids 98 (2017) 201-221.

[39] H. Idrissi, K. Renard, L. Ryelandt, D. Schryvers, P.J. Jacques, On the mechanism of twin formation in Fe-Mn-C TWIP steels, Acta Mater. 58 (2010) 2464-2476.

[40] H. Idrissi, K. Renard, D. Schryvers, P.J. Jacques, On the relationship between the twin internal structure and the work-hardening rate of TWIP steels, Scr. Mater. 63 (2010) 961-964.

[41] H. Chang, M.Y. Zheng, W.M. Gan, K. Wu, E. Maawad, H.G. Brokmeier, Texture evolution of the Mg/Al laminated composite fabricated by the accumulative roll bonding, Scr. Mater. 61 (2009) 717-720.